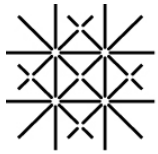


MASTER THESIS



University
of Basel



Fraunhofer
EMI

INTERACTION OF AMPHYPHILIC BOTTLE BRUSH AND STAR POLYMERS WITH A BIOLOGICAL MEMBRANE: A COARSE-GRAINED MOLECULAR DYNAMICS STUDY

Author:

Marco KRUMMENACHER

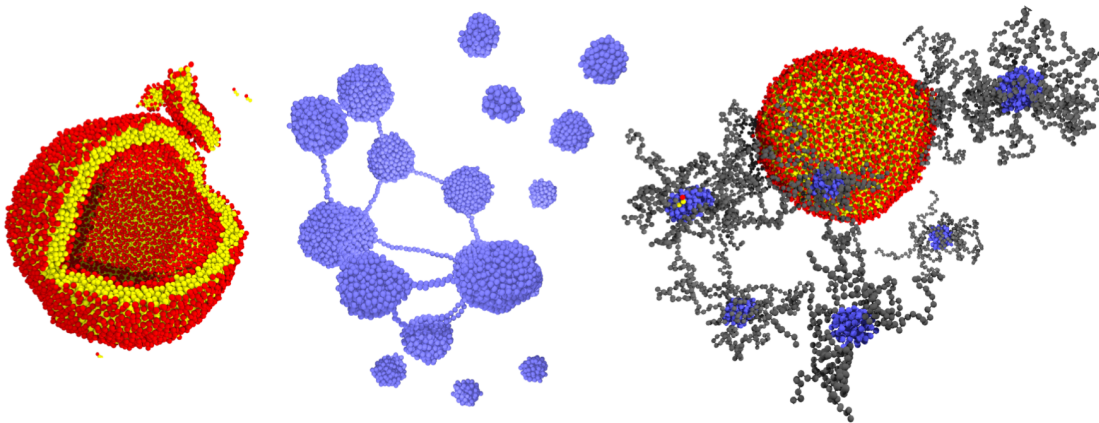
Supervisor:

Priv.-Doz. Dr. rer. nat. habil Martin O. STEINHAUSER

Co-Supervisor:

Prof. Dr. Stefan GOEDECKER

Dr. Deb Sankar DE



September 26, 2019

Abstract

Studying the interaction of branched amphiphilic copolymers with biological membranes is interesting because of two aspects: there is a great interest in using them as drug carriers and microplastic waste is rapidly accumulating in the environment. Molecular dynamics simulations are a powerful tool for a deeper understanding of the interaction of such polymers with a biological membrane in terms of the time- and length scale. Penetration of the hydrophobic parts of amphiphilic star and bottle brush copolymers could be observed. Bottle brush polymers showed a shielding effect the longer the hydrophilic arms are, whereas the penetration of star polymers depended on their functionality f . Therefore, the penetration rate strongly depends on the topology of the amphiphilic copolymers.

Acknowledgements

Throughout the writing of this thesis I have received a great deal of support and assistance. I would first like to thank my supervisor Priv.-Doz. Dr. rer. nat. habil. Martin O. Steinhauser for his expertise and the many answered questions.

I would like to acknowledge Prof. Stefan Goedecker and Dr. Deb Sankar De for the time they spent for the second assesment of this thesis.

Furthermore I would like to thank my colleague Johannes Kalmbach for helping me with many software issues and Udo Ziegenhagel for his great support with the computer cluster.

Last but not least I would like to thank the Fraunhofer Institute for High-Speed Dynamics, Ernst-Mach-Institut to make this project feasible.



Universität
Basel

Philosophisch-Naturwissenschaftliche
Fakultät



Erklärung zur wissenschaftlichen Redlichkeit
(beinhaltet Erklärung zu Plagiat und Betrug)

~~Bachelorarbeit~~ / Masterarbeit (nicht Zutreffendes bitte streichen)

Titel der Arbeit (Druckschrift):

*Interaction of amphiphilic bottle brush and star polymers with
a biological membrane: A coarse-grained molecular dynamics
study*

Name, Vorname (Druckschrift): *Krummenacher Marco*

Matrikelnummer: *14-053-771*

Hiermit erkläre ich, dass mir bei der Abfassung dieser Arbeit nur die darin angegebene Hilfe zuteil wurde und dass ich sie nur mit den in der Arbeit angegebenen Hilfsmitteln verfasst habe.

Ich habe sämtliche verwendeten Quellen erwähnt und gemäss anerkannten wissenschaftlichen Regeln zitiert.

Diese Erklärung wird ergänzt durch eine separat abgeschlossene Vereinbarung bezüglich der Veröffentlichung oder öffentlichen Zugänglichkeit dieser Arbeit.

ja nein

Ort, Datum: *Basel den 27. Sept 2019*

Unterschrift: *M. Krummenacher*

Dieses Blatt ist in die Bachelor-, resp. Masterarbeit einzufügen.

Contents

1	Introduction	7
2	Model	11
2.1	Coarse Graining	11
2.2	Equation of Motion	12
2.3	Particle Interactions	14
2.4	Experimental Set Up	19
3	Molecular Dynamics: An Overview	25
3.1	Reduced Units	25
3.2	Numerical Integration of Differential Equations	26
3.3	Boundary Conditions	29
3.4	Search Algorithms	30
3.5	Limitations	32
4	Measurements	35
4.1	Radial Distribution Function	35
4.2	Cluster Recognition	36
4.3	Penetration Rate	37
5	Results and Discussion	41
5.1	Vesicle Formation	41
5.2	Amphiphilic Copolymers	47
5.3	Interaction of Amphiphilic Copolymers with Vesicles	62
6	Conclusion and Outlook	71
	Appendices	79
A	Vesicle Formation	79

B Amphiphilic Copolymers**83****C Hybrid Systems****91**

1. Introduction

The polarity of water is responsible for the existence of life on earth. It causes hydrophobic and hydrophilic interactions of water with other chemical groups. Biological membranes which separate living organisms from their environment are a result of this effect. Membranes consist of amphiphilic molecules mostly phospholipids which are composed of a relatively short hydrophilic head which is covalently bonded to a long hydrophobic tail. This amphiphilicity causes the self-assembly of a bilayer in aqueous environment, where all hydrophilic heads are pointed towards water, see Fig. 2.1. There are different types of phospholipids in membranes which differ in their chemical structure, but all of them show amphiphilicity. Depending on their concentration, several properties such as the fluidity or the bending angle of membranes are different. Furthermore, a membrane also must be permeable for essential metabolic molecules from the outside and waste products from the inside. Such a semipermeability is ensured by membrane proteins which are able to form channels for very distinct chemical compounds. There are also other integral and peripheral proteins which are not involved in transport but enhance chemical reactions at the surface of membranes. Hence, a biological membrane is a very complex construct of nature including a lot of different components which have very different functionalities. Simulating all properties of a biological membrane is an impossible challenge. Therefore, simulations focus on the key issues which differ in each individual study. In this work the focus lies on the interactions between membranes consisting of lipids and branched amphiphilic copolymers.

Using amphiphilic copolymers in medical applications especially as drug carriers is of high interest [1]. Vesicles composed of amphiphilic copolymers show long-term stability in physiological environment but are usually toxic for cells. Vesicles composed of phospholipids on the other hand show no toxicity but are not long-term stable in a physiological environment. An interesting approach to solve these problems are hybrid vesicles [2] which are composed of both amphiphilic copolymers and lipids. The polymers give the membrane its stability whereas the lipids are responsible for biocompatibility.

Experimental studies are often limited in time scale and spatial resolution so

that it is difficult to gain insight into detailed dynamical properties of systems. Molecular dynamics simulations can complement experimental studies and give a detailed insight into dynamical processes.

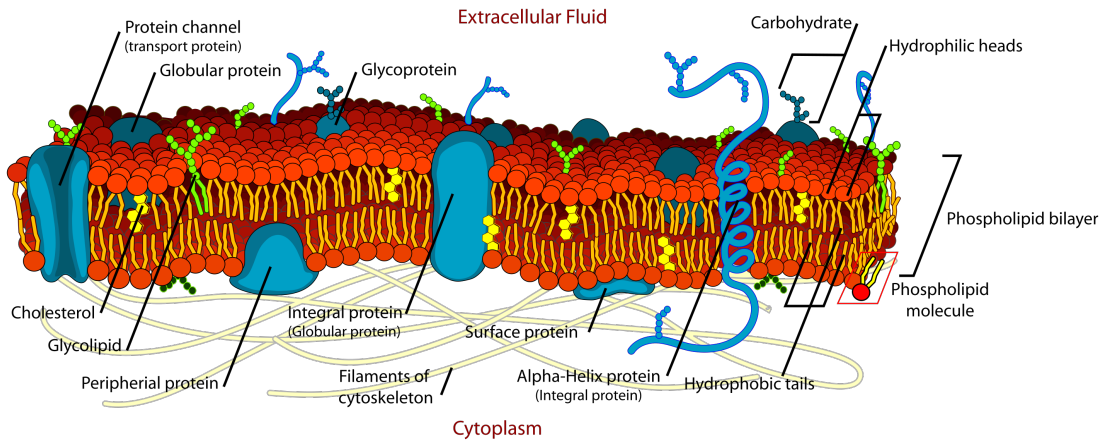


Figure 1.1: Schematic depiction of a biological membrane.

Various computational studies have been performed regarding the self-assembly of amphiphilic copolymers. Different self-assembled formations of poly(acrylic acid)-*b*-polystyrene (PAA-*b*-PS), an AB block copolymer, could be observed, such as vesicle and lamellae formation, depending on the ratio of PS/PAA and the polymer concentration [3]. Amphiphilic bottle brush polymers which had an ABA topology showed membrane formation for a hydrophilic-hydrophobic ratio of 25:75 [4]. A rheological study of amphiphilic tri-block copolymers in water showed micellar microstructures when a strong flow was applied and after a high enough number of integration steps [5]. Gel-networks of amphiphilic star polymers with hydrophobic arm ends showed an increased cluster formation with increased hydrophobic attraction [6]. Hence, amphiphilic copolymer networks show a broad variety of self-assembled structures in simulation studies.

But not only systems consisting of amphiphilic copolymers were studied extensively over the past years but also their interaction with lipids. Raft formation of lipids in a membrane consisting of AB copolymers could be observed depending on the concentration of lipids and the thickness of the polymer membrane [7]. The thicker the membrane, the higher the lipid concentration had to be in order to form rafts. A similar study with a membrane of amphiphilic ABA copolymers showed that raft formation occurred at lower concentration in a bilayer than in a monolayer structures [8]. This can be explained by the im-

miscibility between polymers and lipids in the bilayer configuration.

The detailed understanding of the interaction between polymers and membranes is not only of high interest because of medical applications but also due to the increase of microplastic in the environment. A study in 2018 has found microplastic in the stool of eight people from different continents [9]. The interaction of some of these polymers with a bilayer membrane were presented in a simulation study [10]. Polypropylene and polystyrene were equally distributed inside the bilayer whereas polystyrene showed cluster formation. Not only purely hydrophobic polymers are extensively used in industry but also polymers with amphiphilic topology. They are components in soaps where they are the main ingredient to solve fat in water [11]. Therefore, having on the one hand, the pharmaceutical approach of using amphiphilic polymers as drug carriers and on the other hand the environmental issue, studying the interaction of such polymers with biological membranes is of high interest.

This thesis is structured as follows: first, the model used for the simulations is presented in Chapter 2. The coarse graining approach, solvent free simulation and the force model are presented in more detail. In Chapter 3 an insight into the principles of molecular dynamics is given. The different numerical evaluations are described in Chapter 4 and the corresponding results are presented in Chapter 5. Finally, in Chapter 6 a review of the results of this work as well as a short outlook is provided.

2. Model

Molecular dynamics simulations are based on a potential model which determines the interactions between particles. Depending on the purpose of the simulation, different methods on different length- and time scales are used. In simulations regarding a very small scale, all atom or even quantum models are applied. On the mesoscale level, as in this work, usually coarsened models are used whereas for large scales finite element methods are applied. In the first section the term *coarse graining* is described in more detail. Section 2.2 describes the usage of Newton's equation of motion in simulations. In Sec. 2.3 an overview of the potentials which are used in this work is provided. The simulation procedure is described in the last Section 2.4.

2.1 Coarse Graining

Biological membranes are mainly composed of phospholipids which determine their bilayer structure. Phospholipids are amphiphilic macromolecules composed of a hydrophilic head group and a hydrophobic tail which are covalently connected by a phosphorus group. There are many different types of phospholipids in nature and the detailed chemical structure of their head and tail group is very different, but all show amphiphilicity. Since in the simulations, in this work, the focus lies on the amphiphilic interactions between lipids and polymers, a highly coarse-grained model is applied in contrast to other models based on the MARTINI force field [12]. The lipids in our model are represented by three beads: one bead represents the hydrophilic head and two beads the hydrophobic tail, see Fig. 2.1 (a). Therefore, certain chemical properties are lost. Using a highly coarsened-grained model raises computational efficiency and, hence, more particles can be simulated. Three bead models have already been successfully tested for membrane simulations and are suitable to test a variety of physical properties, including self-assembly, fusion, bilayer melting, lipid mixtures, rafts, and protein-bilayer interactions [13, 14].

The polymers considered in this work, as well as the membrane, are composed

of hydrophobic and hydrophilic particles. Two general polymer topologies were simulated: bottle brushes and star polymers, see Fig. 2.1 (b). For the bottle brush polymers two different amphiphilic profiles were studied. One amphiphilic profile consists of a hydrophobic backbone and hydrophilic arms, which is referred to *bottle brush polymer type A*. The other amphiphilic profile is a bottle brush polymer which is partially hydrophobic. This profile is referred to *bottle brush polymer type B* in this work. The center of star polymers is always hydrophilic and some monomers towards the end of the arms are hydrophobic, see Fig. 2.1.

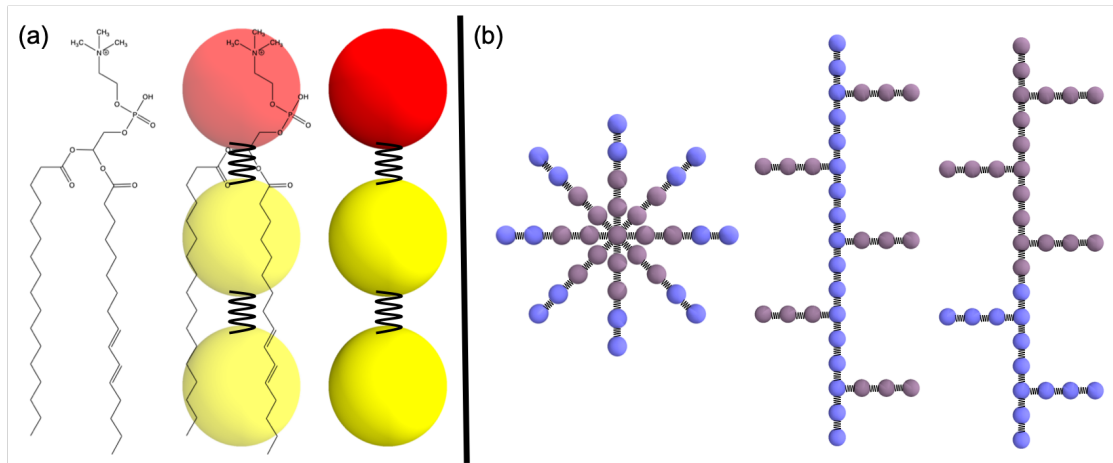


Figure 2.1: Schematic depiction of the coarse-grained model. (a) Bead-spring model of the lipids. The hydrophobic tails are depicted in yellow color whereas the hydrophilic heads are in red color. (b) Bead-spring model of the amphiphilic bottle brush and star polymers. The hydrophobic parts are depicted in blue color whereas the hydrophilic parts are in grey color.

2.2 Equation of Motion

Although some quantum mechanical effects are implicitly built in the potentials e.g. the Pauli repulsion, see Sec. 2.3, the particles move according to classical mechanics. Hence, the motion of a particle i with mass m_i is given by Newton's equation of motion:

$$\mathbf{F}_i = m_i \frac{d\mathbf{r}_i^2}{dt^2}, \quad (2.1)$$

where \mathbf{F}_i is the force acting on the i^{th} particle, r_i is its position and t denotes time. The forces acting on each particle, which are described in Sec. 2.3, are determined by the potential energy $U(\mathbf{r})$ by the following relation

$$\mathbf{F}_i^{\text{pot}} = -\vec{\nabla}_{\mathbf{r}_i} U_i^{\text{tot}}(\mathbf{r}), \quad (2.2)$$

where $\vec{\nabla}_{\mathbf{r}_i} = \left(\frac{dU_i^{\text{tot}}(\mathbf{r})}{dx_i}, \frac{dU_i^{\text{tot}}(\mathbf{r})}{dy_i}, \frac{dU_i^{\text{tot}}(\mathbf{r})}{dz_i} \right)$. The model used in this work is solvent free and integrated in a canonical NVT-ensemble. Because in a NVT-ensemble the temperature is constant the initial velocities of the particles have to satisfy the equipartition theorem:

$$\left\langle \frac{1}{2} m_i |\mathbf{v}_i^0|^2 \right\rangle = \frac{3}{2} k_B T. \quad (2.3)$$

Hydrophobic interactions caused by the solvent are described by an additional attractive potential acting between hydrophobic particles. Other interactions of the particles with the solvent caused by Brownian motion can be described by Langevin Dynamics [15, 16] which couples the system to a heat bath. This is done by splitting the Brownian force into a slowly acting friction force $\mathbf{F}_\gamma(t)$ of Stokes type and a fast fluctuating stochastic force $\mathbf{R}_i(t)$. The total force acting on a particle has then the following form

$$\mathbf{F}_i^{\text{tot}} = -\vec{\nabla}_{\mathbf{r}_i} U_i^{\text{tot}}(\mathbf{r}) + \gamma \frac{d\mathbf{r}_i}{dt} + \mathbf{R}_i(t), \quad (2.4)$$

where $\gamma \frac{d\mathbf{r}_i}{dt} = \mathbf{F}_\gamma(t)$ and γ is the friction coefficient. The properties of the stochastic Langevin force are given by the fluctuation dissipation theorem [17]:

$$\langle \mathbf{R}_i(t) \cdot \mathbf{R}_j(t') \rangle = 6k_B T \gamma \delta_{i,j} \delta(t - t'), \quad (2.5)$$

where T is the temperature and k_B is the Boltzmann constant. Furthermore, since on average no momentum is transferred from the solvent to the particles, the stochastic force has also to satisfy

$$\langle \mathbf{R}_i(t) \rangle = 0. \quad (2.6)$$

Therefore, this stochastic force is of Gaussian type, also called white noise. The friction force constant can be obtained by hydrodynamic calculations for sufficiently large spherical particles [17] and is given by

$$\gamma = 6\pi\eta_s a, \quad (2.7)$$

where a is the radius of the particles and η_s the viscosity of the solvent.

The total force in Eq. 2.4 is used to propagate the positions and velocities of the particles in time. For this purpose the velocity Verlet algorithm is used which is described in Sec. 3.

2.3 Particle Interactions

The total potential energy U of a N -body system can be written as

$$U(\mathbf{R}) = \sum_i^N U_1(\mathbf{r}_i) + \sum_i^N \sum_{j>i}^N U_2(\mathbf{r}_i, \mathbf{r}_j) + \sum_i^N \sum_{j>i}^N \sum_{k>j}^N U_3(\mathbf{r}_i, \mathbf{r}_j, \mathbf{r}_k) + \dots, \quad (2.8)$$

where $U_1, U_2, U_3 \dots$ describe the interactions between particles and external fields and between themselves. External fields could for example be of electrostatic or magnetic nature but are ignored in this work except for reflecting boundary conditions, see Sec. 3.3. Interactions of more than second order are usually neglected due to computational efficiency. The pair potentials presented in this section and used for the simulation in this work are the Lennard-Jones (LJ) potential to mimic soft spheres, an attractive potential to simulate hydrophobic effects and a spring potential to describe covalent bonds. A bending potential which is introduced to stretch the bonds is the only potential of third order. There are also other potentials used to describe certain properties such as Coulomb or dipole potentials but they are not used in this work. A more detailed insight to those interactions can be found in Ref. [18]. In general one distinguishes between intra- and intermolecular potentials. Intramolecular potentials act between the particles of one molecule. Intermolecular potentials are used to describe the interactions between molecules. In the following section, the intermolecular potentials are described first followed by the intramolecular potentials.

Lennard-Jones potential

In coarse-grained simulations the particles are described as mass points. In order to characterize excluded volume effects i.e. simulating soft beads, the most widely used potential is the LJ-(6-12) potential:

$$U_{LJ}(r_{i,j}) = 4 \epsilon \left[\left(\frac{\sigma}{r_{i,j}} \right)^{12} - \left(\frac{\sigma}{r_{i,j}} \right)^6 \right], \quad (2.9)$$

where ϵ and σ are the reduced energy and length unit and $r_{i,j} = |\mathbf{r}_i - \mathbf{r}_j|$ is the distance of two mass points. Energy parameter ϵ determines the depth of the potential whereas the distance parameter σ determines the length scale. The repulsive $r_{i,j}^{-12}$ part can be explained by the Pauli repulsion principle from quantum mechanics, which shows an exponential decay. Due to the fact that exponential functions are computationally expensive, a less expensive polynome

is chosen for the repulsion term. The attractive r_{ij}^{-6} term describes long ranged van der Waals interactions. Since for computational efficiency, potentials should be kept short ranged in order to keep the force calculations at a minimum, a short ranged version was introduced by Weeks-Chandler-Anderson [19] where the potential is cut-off at its minimum value $r_c = \sqrt[6]{2}$ and shifted by ϵ so that it is purely repulsive:

$$U_{WCA}(r_{ij}) = \begin{cases} 4 \epsilon \left[\left(\frac{\sigma}{r_{ij}} \right)^{12} - \left(\frac{\sigma}{r_{ij}} \right)^6 \right] + \epsilon & r_{ij} < r_c = \sqrt[6]{2}\sigma, \\ 0 & \text{otherwise.} \end{cases} \quad (2.10)$$

In Fig 2.2 both the LJ-(6-12) and the WCA-approximation described by Eq. 2.9 and 2.10, respectively, are depicted for $\epsilon = \sigma = 1.0$.

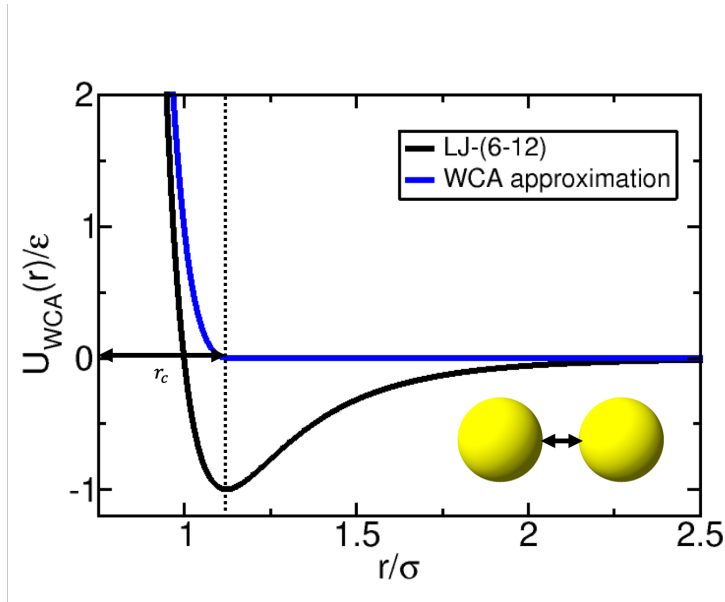


Figure 2.2: The Lennard-Jones potential (black) and the Weeks-Chandler-Anderson approximation (blue). The WCA approximation in this work is used to describe excluded volume effects and therefore transform the mass points into soft beads.

Hydrophobic Potential

In order to mimic hydrophobic interactions in a solvent free model, an attractive potential is introduced between hydrophobic beads. Several attractive potentials based on the LJ-potential have been proposed and successfully used in

simulations [6, 20, 21]. However, in this work a cosine shaped potential was used which was proposed in Ref. [13]:

$$U_{ATTR}(r_{i,j}) = \begin{cases} -\epsilon & 0 < r_{i,j} < r_c, \\ -\epsilon \cos^2\left(\frac{\pi(r_{i,j}-r_c)}{2h_c}\right) & r_c < r_{i,j} < r_c + h_c, \\ 0 & \text{otherwise,} \end{cases} \quad (2.11)$$

where h_c determines the range of the attraction and r_c the cut-off radius of the WCA potential. Although this potential is very different to the LJ-based attractive potential, no significant difference in the results could be observed in simulations but the cosine shaped potential is preferable due to its slightly shorter interaction range [21]. Figure 2.3 shows a plot of the cosine shaped attractive potential with different attraction ranges h_c .

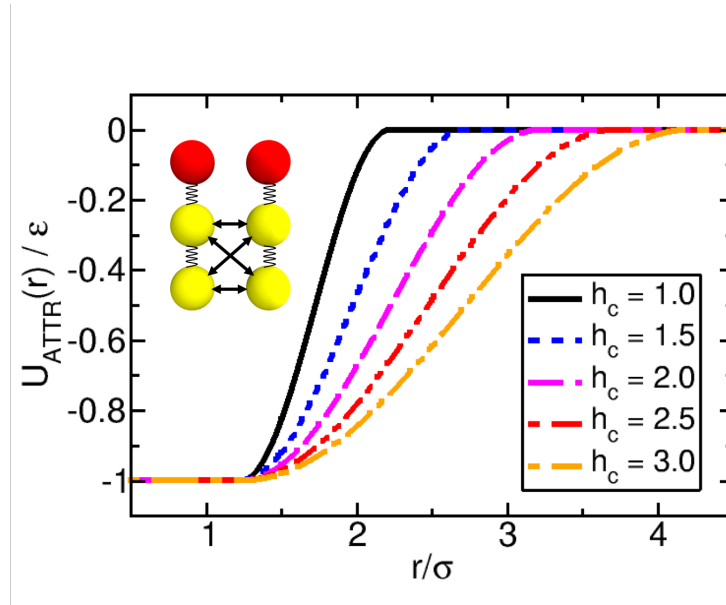


Figure 2.3: Cosine shaped attractive potential described in Eq. 2.11 with different attraction range h_c . This potential simulates the hydrophobic attraction.

FENE Potential

The simplest approach to characterize covalent bonds in simulation is a harmonic spring model

$$U_{HARM}(r_{i,i+1}) = \frac{\kappa_{HARM}}{2} (|\mathbf{r}_i - \mathbf{r}_{i+1} - l_0|)^2, \quad (2.12)$$

where \mathbf{r}_i and \mathbf{r}_{i+1} are the coordinates of the two connected beads, l_0 is the equilibrium bondlength and κ_{HARM} is the harmonic spring constant. However, since the bondlength of covalent bonds is not very well described by a harmonic potential, often a Finitely Extensible Non-linear Elastic (FENE) potential is used which restricts the bondlength to a maximum threshold [22]:

$$U_{FENE}(r_{i,i+1}) = \begin{cases} -\frac{\kappa_{FENE}}{2} R_0^2 \ln \left(1 - \frac{r_{i,i+1}^2}{R_0^2} \right) & r < R_0, \\ 0 & \text{otherwise,} \end{cases} \quad (2.13)$$

where $\kappa_{FENE} = 30 \epsilon/\sigma^2$ is the stiffness, $R_0 = 1.5\sigma$ is the maximum bondlength and $r = |\mathbf{r}_i - \mathbf{r}_{i+1}|$. In Fig. 2.4 a plot of Eq. 2.13 is shown with $\epsilon = \sigma = 1$. Together with the LJ-(6-12) potential a resulting equilibrium bondlength of about $l_0 \approx 0.97$ in reduced units is achieved.

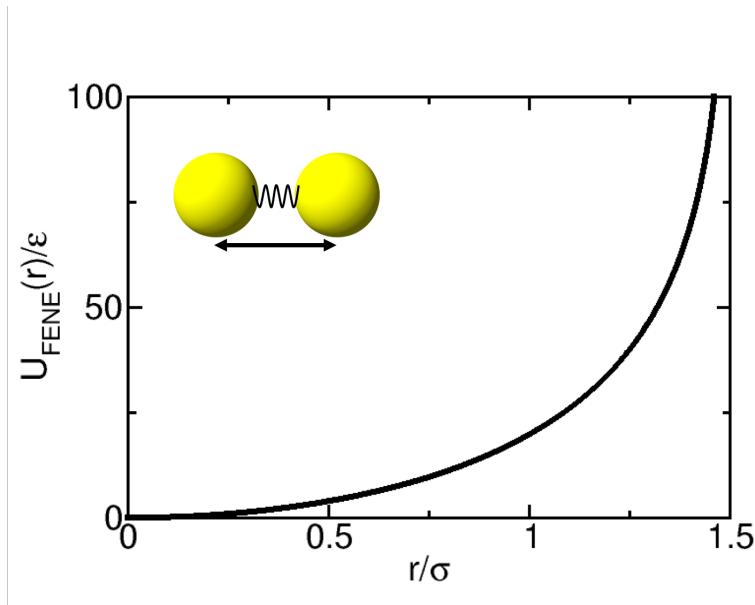


Figure 2.4: The FENE potential with $\kappa_{FENE} = 30 \epsilon/\sigma^2$ and $R_0 = 1.5\sigma$ with $\epsilon = \sigma = 1$. Together with the LJ-(6-12) potential an elastic potential with an equilibrium bondlength of $l_0 \approx 0.97$ is achieved.

Bending Potential

Since phospholipids are usually not fully flexible but rather stiff, a bending potential which stretches the lipids is introduced. Such a bending potential can

be described as in Ref. [13] as a pair potential between the k^{th} and the $k^{\text{th}} + 2$ particle

$$U_{BEND}(r_k) = \frac{\kappa_{BEND}}{2}(r_k - 4\sigma), \quad (2.14)$$

where $r_k = |\mathbf{r}_k - \mathbf{r}_{k+2}|$. Since in this pair potential, the motion of the particle r_{k+1} is completely neglected, a harmonic bending potential as described in Ref. [23] was used in this work. This potential has the form

$$U_{BEND} = \frac{\kappa_{BEND}}{2}(\mathbf{u}_{i+1} - \mathbf{u}_i)^2 = \kappa_{BEND}(1 - \cos \theta_i), \quad (2.15)$$

where $\mathbf{u}_i = \mathbf{r}_{i+1} - \mathbf{r}_i / |\mathbf{r}_{i+1} - \mathbf{r}_i|$, $\theta_i = \sphericalangle(r_{i,i+1}, r_{i+1,i+2})$ and κ_{BEND} determines the stiffness of the bond. In Fig. 2.5 the bending potential for $\kappa_{BEND} = 10 \epsilon / \sigma^2$ is depicted. Two equilibrium positions at $\theta = 0$ and $\theta = \pi$ can be observed. The latter equilibrium position is prohibited by the LJ-potential since it would mean that particle i and $i + 2$ would be at exactly the same position.

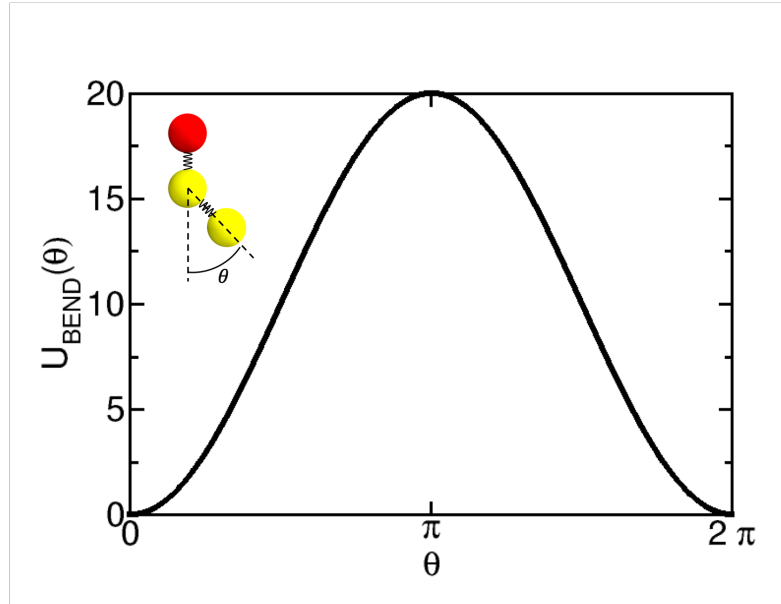


Figure 2.5: Bending potential described in Eq. 2.15 with $\kappa = 10 \epsilon / \sigma^2$. Two equilibrium positions at $\theta = 0$ and $\theta = \pi$ can be observed whereas latter is prohibited by the LJ-potential.

The total potential energy is then given by the sum of Eq. 2.10, 2.11, 2.13 and

2.15:

$$\begin{aligned}
 U_{TOT} = & \underbrace{\sum_{i=1}^{N_{tot}-1} \sum_{j=i+1}^{N_{tot}} U_{WCA}(r_{i,j}) + \sum_{i=1}^{N_{hp}-1} \sum_{j=i+1}^{N_{hp}} U_{attr}(r_{i,j})}_{\text{Intermolecular Potentials}} + \\
 & \underbrace{\sum_{i=1}^{N_{bond}-1} \sum_{j=i+1}^{N_{bond}} U_{FENE}(r_{i,i+1}) + \sum_{i=1}^{N_{bond}/3} U_{BEND}(\theta_i)}_{\text{Intramolecular Potentials}},
 \end{aligned} \tag{2.16}$$

where N_{tot} is the total number of particles, N_{bond} the number of particles which are covalently bond to each other and N_{hp} the number of particles which attract each other due to hydrophobicity.

2.4 Experimental Set Up

As in real experiments computer *experiments* follow several distinct steps, see Fig 2.6. First of all, the molecules which are used in the simulation are generated, which is the counterpart of synthesizing polymers and lipids. In a second step, a warm-up procedure with respect to the LJ- and bending potential is performed. Before mixing the lipids and polymers together, a prerun is performed where the two different molecules reach equilibration separately. After that the interaction between the molecules is switched on and a productive run is performed. After the systems have equilibrated, evaluations are performed. The results of these evaluations are presented in Sec. 5.

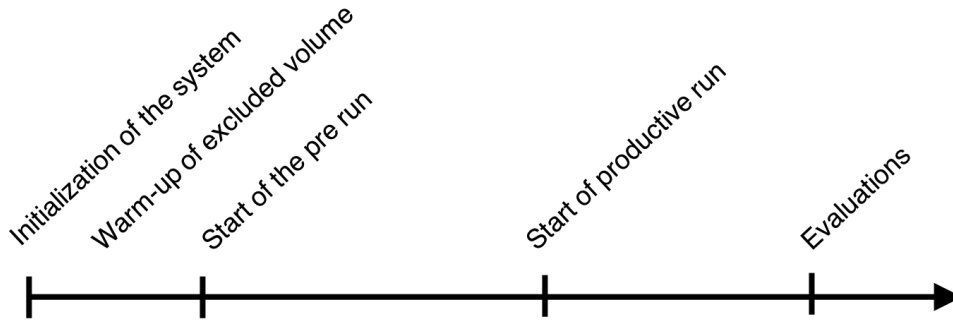


Figure 2.6: Simulation timeline which shows the procedure of the simulation of hybride systems.

Initialization

The initial configuration of the chains is generated in a random process, one particle at the time. An algorithm which initializes the chains, places the monomers into the simulation box as a non-reversible random walk [24]. The first particle i of the chain is placed randomly in the simulation box. The second one ($i + 1$) is also placed in a random direction but with a distance of $d_0 = 0.97\sigma$ with respect to the first particle. Particle $i + 2$ and all further particles are also placed randomly but are only accepted if $d_{i,i+2} > r_{excluded} = 1.02\sigma$, see Fig. 2.7 (a). However, this algorithm does not ensure that particles which are far away from each other (with respect to the particle index i) or particles from different chains show singularities with respect to the LJ-potential. Therefore, starting the simulation run may lead to singularities in the potentials. In order to avoid singularities in the potential and, hence, numerical instabilities, a warm up procedure is first applied before starting the simulation run, see Fig. 2.7 (b).

Membrane or vesicle formation can be enhanced by shrinking the space in the random initialization either in z-direction (enhancing membrane formation) or all directions (enhancing vesicle formation). This results in a higher density of the lipids at the beginning of the simulation. Hence, the lipids are closer to each other and more hydrophobic interactions occur which, together with reflecting boundary conditions, see Sec. 3.3, speeds up the formation of membranes and vesicles respectively.

The initialization of hybrid systems, where the interaction between branched amphiphilic polymers and lipids is examined, the simulating box is divided into two subspaces. First, a subbox is created where only lipids are placed, see Fig. 2.8 (a). The branched molecules are then initialized in a shell around the subbox of the lipids, which has at least the size of two average lengths of the backbone which, for a non-reversible random walk is $\sqrt{N_{backbone}}$. In order to ensure that the whole branched polymer is placed in the subbox, the first particle of a backbone is initialized within a threshold distance of one average backbone length. However, this procedure ensures only on average that all particles of the backbone are inside the simulation box after a non-reversible random walk. Since reflecting boundary conditions are applied we need to ensure that all particles are inside the box after the initialization. Therefore a Monte Carlo sampling was applied, see Fig. 2.8 (b). If all particles of a branched polymer are placed inside the simulation box, it is accepted and the next polymer is initialized. If the condition is not satisfied, the polymer initialization is not accepted and another polymer is randomly initialized. This procedure is repeated until all particles of all polymers are initialized inside the simulation box. Such a Monte Carlo sampling ensures on the one hand that all particles of the polymer are placed inside the simulation box, but also on the other hand, that the poly-

mers are still initialized randomly. The acceptance rate of this algorithm initializing bottle brush polymers with $N_{arm} = 10$ and a backbone of $N_{backbone} = 100$ is displayed in Fig. 2.9. The longer the arms are, the lower is the acceptance rate. This fact can be explained by the decreasing probability of an arm to be completely inside the box with increasing armlength.

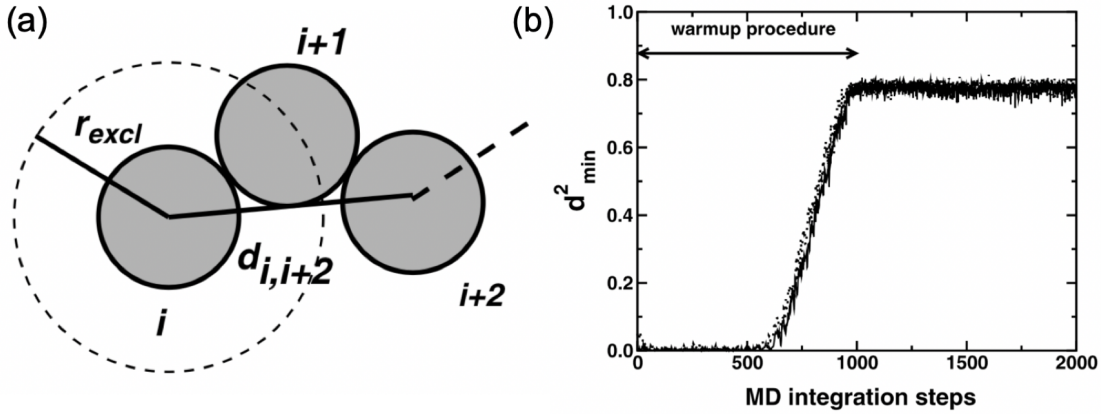


Figure 2.7: (a) Initialization of the chains with a non reversible random walk algorithm. (b) Warmup of the LJ potential to avoid numerical instabilities at the beginning of the simulation. The figure is taken from Ref. [25].

Warm-up

As mentioned before it may happen, that some particles are very close together in the initial configuration, what can lead to singularities in the force calculation. In order to avoid numerical instabilities, a warmup is performed where the LJ- and the bending potential are increased successively until they act in their full form on the particles.

The warmup of the LJ potentials is done in the following manner as described in Ref. [25]. In a first step the minimum distance d_{min} between all particles is calculated. Since this calculation has only to be performed once it does not contribute a lot of computational effort compared to the whole simulation. However, usually the minimum distance d_{min} is in the order of $1 \cdot 10^{-4}$ and taking a safty margin of two order of magnitudes one can simply take $d_{min} = 1 \cdot 10^{-6}$. As a second step the LJ-potential is successively increased during n_{warmup} integration steps which is usually about 1000. Instead of taking the actual distance r of the calculation, a rescaled distance of

$$r' = r + \Delta d - \frac{n}{n_{warmup}} \Delta d \quad (2.17)$$

is taken, where n is the actual time step, r the actual distance and $\Delta d = r_{cut}^{max} - d_{max}$. The distance r_{cut}^{max} is the largest cut off of all non bonded interactions which is in our case $r_{cut}^{max} = r_c$, since no hydrophobic attraction is applied during the warm-up process. In Fig. 2.7 (b) the successive increase of LJ potential during the warmup procedure can be observed.

Not only the LJ- but also the bending potential U_{BEND} can lead to singularities after initialization. Therefore also a warmup procedure for this potential is introduced. This is done by successively increasing the stiffness κ_{BEND} during n_{warmup} integration steps by employing $\kappa_{BEND} \cdot n / n_{warmup}$. During the warmup procedure the FENE potential acts with its entire strength since there are no singularities due to the random walk initialization.

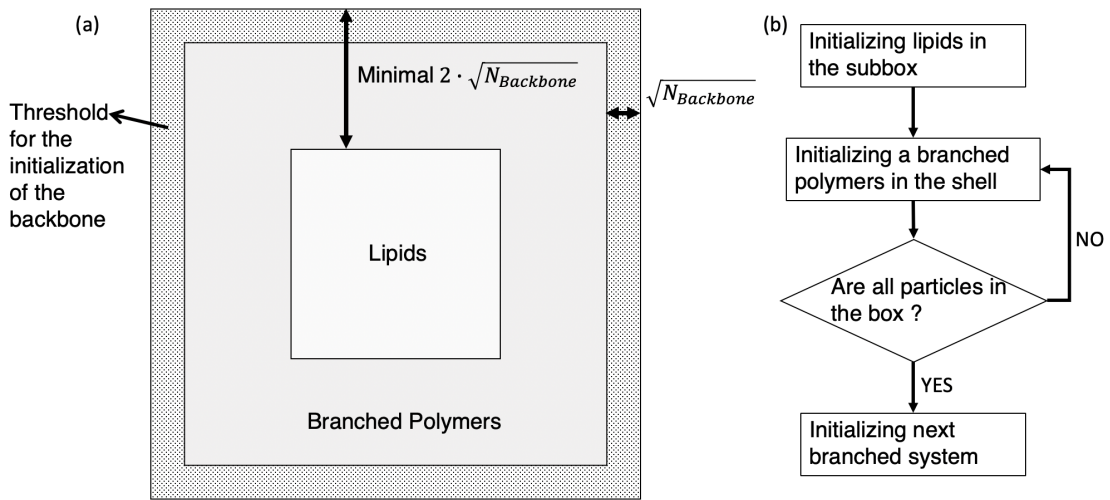


Figure 2.8: Initialization process of hybrid systems: (a) subdivision of the simulation box and (b) Monte Carlo sampling of the amphiphilic branched polymers.

Prerun

In order to come a real experiment as close as possible a prerun is performed to equilibrate the lipids and the polymers separately. This can be done by distinguishably switching on and off the hydrophobic attraction. For n_{eq} integration steps the hydrophobic attraction potential U_{ATTR} is switched off between the polymers and the lipids. All other potentials, including the attractive potential between lipid-lipid and polymer-polymer are switched on. This ensures that membranes and vesicles can self-assemble before the interactions of them with amphiphilic polymers is studied. Furthermore, in order to speed up the self as-

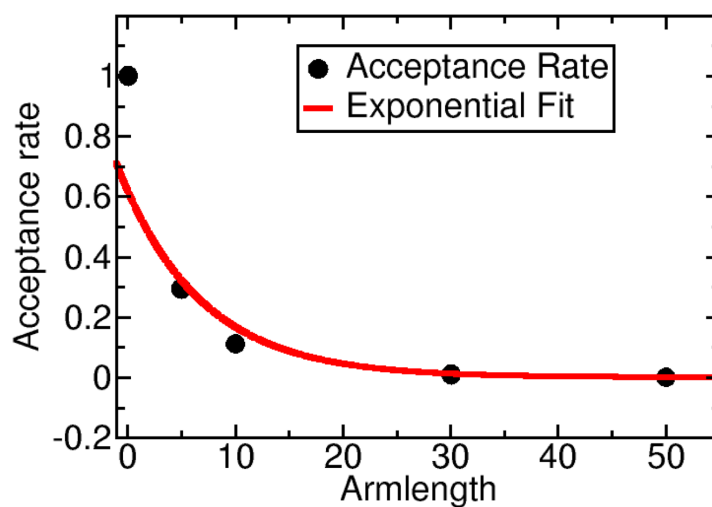


Figure 2.9: Acceptance rate of the Monte Carlo algorithm which was used for the initialization.

sembly of lipids, during the prerun, periodic boundary conditions are applied to the subbox where the lipids were initialized, see Sec. 3.3. Thinking of this as a real experiment, first the membrane is formed in one vessel whereas the polymers are prepared in another. When both systems, the lipids and the polymers, have reached equilibrium, the attractive hydrophobic potential between lipids and polymers is switched on and the two vessels are mixed together.

3. Molecular Dynamics: An Overview

Molecular dynamics (MD) is a particle based simulation technique. The particles in the simulation move according to Newton's classical equation of motion, see Eq. 2.1. MD simulations are deterministic, since after having initialized positions and momenta of all particles, these two quantities can be calculated for any point in time in the past and the future [26]. There are other techniques which in contrast to MD are probabilistic, e.g. quantum mechanics or Monte-Carlo (MC) methods [27]. Both methods, MD and MC methods take advantage of the ergodic hypothesis [28], which states that the time average is the same as the ensemble average, in order to describe equilibrated states. While MC methods take a statistically large ensemble to calculate equilibrium states, MD uses the average over a large number of timesteps. During this work, only MD simulations were performed. Therefore, the focus on the following section lies in the theoretical description of MD simulations.

The very first MD simulation was performed in 1957, see Ref. [29]. It was about an examination of the phase transition of a two dimensional hard sphere system. The further development of MD was closely related to the increasing computational power in the last decades. Since this is not a thesis about the history of MD the reader is referred to Ref. [26] for more historical facts.

The following part is organized as followed: In Sec. 3.2 the numerical integration of the equation of motion is described. Sec. 3.3 and 3.4 give an introduction to boundary conditions and search algorithms respectively. Last but not least, in Sec. 3.5 some limitations of MD simulations are mentioned.

3.1 Reduced Units

Processing very small and very large numbers in computers lead to significant numerical rounding errors. In order to avoid them dimensionless so called reduced units are introduced. The energy and the length are scaled according to

ϵ and to σ respectively. The reduced energy and length are

$$E^* = \frac{E}{\epsilon} \quad \text{and} \quad \mathbf{r}^* = \frac{\mathbf{r}}{\sigma}. \quad (3.1)$$

The force \mathbf{F} becomes

$$\mathbf{F}^* = \frac{\sigma}{\epsilon} \mathbf{F} \quad (3.2)$$

in reduced units and the time is rescaled according to

$$t^* = \sqrt{\frac{\epsilon}{m\sigma^2}} t. \quad (3.3)$$

Hence, the temperature is in reduced units

$$T^* = \frac{k_B T}{\epsilon}, \quad (3.4)$$

since $k_B T$ has the dimension of energy. These reduced units reduce numerical rounding errors tremendously.

3.2 Numerical Integration of Differential Equations

Newton's equation of motion (Eq. 2.1) is an ordinary differential equation of second order. This equation is continuous and in order to solve it numerically it has to be discretized. Instead of taking an infinite set of the independent variables position \mathbf{r} and time t only a finite set is taken. The finiteness of the variables i.e the discretization enables computers to integrate ordinary differential equations. Not only the two variables position and time become discontinuous but also its derivative i.e the differential quotient.

There are several numerical methods to integrate ordinary differential equations which have its advantages and disadvantages. In this section a very good and a very bad integrator to solve Newtons equation of motion will be discussed namely the velocity Verlet and the Euler algorithm. The following section is inspired from Ref. [26].

Euler Algorithm

The simplest approach to numerically integrate ordinary differential equation is based on using a Taylor expansion

$$\mathbf{r}(t + \Delta t) = \mathbf{r}(t) + \frac{d\mathbf{r}(t)}{dt} \Delta t + \frac{1}{2!} \frac{d^2\mathbf{r}(t)}{dt^2} \Delta t^2 + \frac{1}{3!} \frac{d^3\mathbf{r}(t)}{dt^3} \Delta t^3 + \dots, \quad (3.5)$$

where Δt represents a finite time step. Since calculating an infinite sum is computationally inefficient a truncated version can be used where an approximate integration is performed so that the Taylor expansion becomes

$$\mathbf{r}(t + \Delta t) = \mathbf{r}(t) + \frac{d\mathbf{r}(t)}{dt}\Delta t + \frac{1}{2!} \frac{d^2\mathbf{r}(t)}{dt^2}\Delta t^2. \quad (3.6)$$

However, this leads to severe truncation errors. In Fig. 3.1 the position and the energy of the integration of a one dimensional harmonic oscillator with the Euler algorithm are shown for different time steps Δt . The larger the time step Δt is the more severe becomes the position and energy drift. Of course it can be argued that a sufficiently small time step leads to a negligible error. However, this would restrict the simulation in the time scale drastically. Furthermore, the algorithm is also not time reversible and does not conserve the phase space volume, what is a consequence of the energy drift. Therefore, the Euler algorithm is not appropriate for MD simulations.

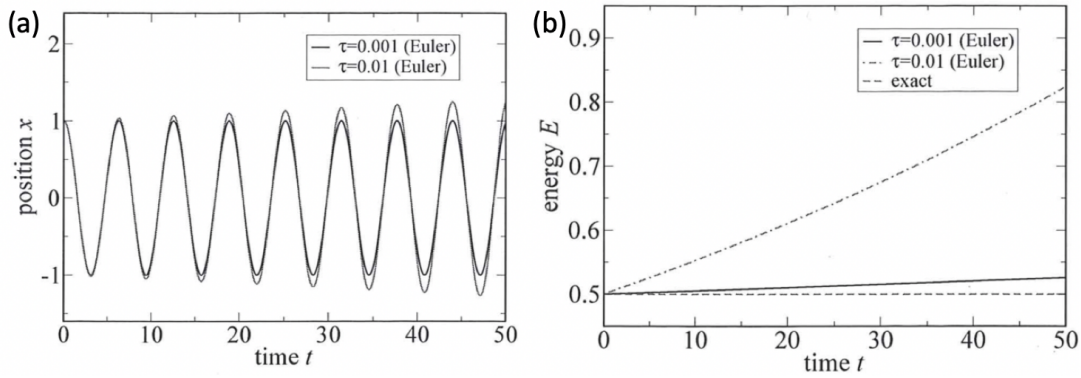


Figure 3.1: Euler algorithm applied to a one dimensional harmonic oscillator with different time steps Δt . (a) Position drift of the Euler algorithm and (b) energy drift for different timesteps. The figure is taken from Ref. [26].

Verlet Algorithm

The Verlet algorithm was invented in 1967 by Loup Verlet [30]. The method is based on using discrete difference operators which is for the second derivative

$$\left[\frac{d^2\mathbf{r}_i}{dt^2} \right]_n := \frac{1}{\Delta t} \left[\mathbf{r}_i^{n+1} - 2\mathbf{r}_i^n + \mathbf{r}_i^{n-1} \right], \quad (3.7)$$

where $\mathbf{r}_i^{n+1} = \mathbf{r}(t + \Delta t)$. Inserting Eq. 3.7 into Newton's equation of motion (Eq. 2.1) yields

$$\mathbf{r}_i^{n+1} = 2\mathbf{r}_i^n - \mathbf{r}_i^{n-1} + \frac{\Delta t^2 \mathbf{F}_i^n}{m_i}, \quad (3.8)$$

where \mathbf{F}_i^n is the force acting on the i^{th} particle and m_i is its mass. The velocities are calculated using the central difference method

$$\mathbf{v}_i^n = \left[\frac{d\mathbf{r}_i}{dt} \right]_n := \frac{\mathbf{r}_i^{n+1} - \mathbf{r}_i^{n-1}}{2 \Delta t}. \quad (3.9)$$

The original Verlet algorithm has two major disadvantages: (i) two numbers of very different size are added (the last term is multiplied by the small number Δt^2) and (ii) the velocities are not calculated directly by this integration scheme, see Fig. 3.2 (a). (i) results in numerical rounding errors. In order to avoid those errors a modified version of the original algorithm the so called Verlet leapfrog algorithm [31] can be applied which is algebraically identical. Different to the original algorithm, the velocities are calculated first and at time $t_{n+1/2}$, see Fig. 3.2 (b). Hence the velocities are updated according to

$$\mathbf{v}_i^{n+1/2} = \mathbf{v}_i^{n-1/2} + \frac{\Delta t \mathbf{F}_i^n}{m_i}, \quad (3.10)$$

and the positions are afterwards determined as

$$\mathbf{r}_i^{n+1} = \mathbf{r}_i^n + \Delta t \mathbf{v}_i^{n+1/2}. \quad (3.11)$$

Since the time step Δt is not squared anymore in this version of the Verlet algorithm numerical rounding errors can be reduced. However, the probably most often used version in MD simulation is the velocity Verlet algorithm [32]. It shows long term stability in terms of rounding errors and all quantities including the velocities are calculated at the same time. Solving Eq. 3.9 for \mathbf{r}_i^{n-1} and substituting the result into Eq. 3.8 yields

$$\mathbf{r}_i^{n+1} = \mathbf{r}_i^n + \Delta t \mathbf{v}_i^n + \frac{\Delta t^2 \mathbf{F}_i^n}{2m_i}. \quad (3.12)$$

Solving this equation for \mathbf{v}_i^n and adding the corresponding expression for \mathbf{v}_i^{n+1} (by substituting n with $n + 1$) results in an expression for the velocity which is not dependent on the position update:

$$\mathbf{v}_i^{n+1} = \mathbf{v}_i^n + \frac{(\mathbf{F}_i^{n+1} + \mathbf{F}_i^n)\Delta t^2}{2m_i}. \quad (3.13)$$

In this work all simulations were performed with the velocity Verlet algorithm with a timestep of $\Delta t = 0.01$. Further to the above mentioned advantageous and which are generally true for all three different Verlet integration schemes are:

- robustness with respect to the time step Δt ,
- time reversibility,
- conservation of the phase space volume i.e energy conservation.

Even though the algorithm described above shows very good properties, exact calculations of single trajectories in an N-body system are not possible. Even small numerical rounding errors result in trajectories which differ tremendously from its correct ones. This general problem of chaotic systems is called Lyapunov instability [33]. However, MD calculations give still representative results since for evaluations averages over time are calculated.

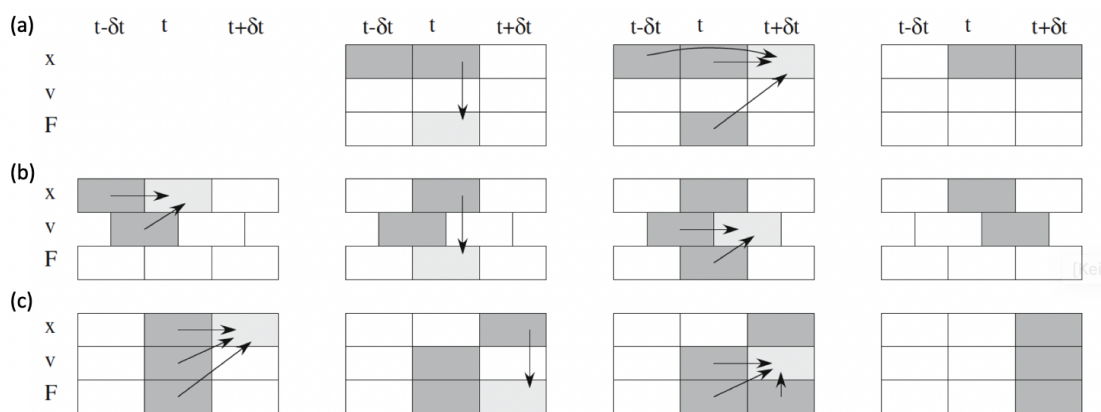


Figure 3.2: Graphical depiction of the different variants of the Verlet algorithm: (a) Original Verlet algorithm, (b) Leapfrog Verlet algorithm and (c) Velocity Verlet algorithm. The figure is according to Ref. [26].

3.3 Boundary Conditions

In MD simulations only a small number of particles can be represented. In order to avoid artificial surface effects, caused by particles which are not surrounded by other particles in any direction, usually periodic boundary conditions (PBC) are introduced, which enable to simulate bulk systems. The cubic simulation

box is repeated in all 26 directions, see Fig. 3.3 (a) for a two dimensional scheme, containing duplicates of each particle. If a particle i leaves the original simulation box at one side, one of its images i' enters on the opposite side. This is done by adding or subtracting multiples of the box length L to the x, y or z -coordinate. Duplicating the simulation box in all 26 directions requires a lot of working storage. Instead, the simulation box can be divided into subcells as described in Sec. 3.4 and only the outer subcells are duplicated into so-called ghost cells i.e. in a layer of subcells surrounding the simulation box.

For all potentials described in Sec. 2.3 a cut-off radius was introduced. Not only speeds this up the simulation but it does also prevent particles to interact with its ghost. However, long range potentials such as the Coulomb potential usually obey no cut-off radius. Therefore, for long-range forces only energy contributions are taken into account of particles which are within a cutoff radius of $L_B/2$, where L_B is the box length. This so called minimum image convention prevents that particles interact with its image and each particle interacts with at most $(N - 1)$ other particles.

In order to speed up the formation of flat membranes and vesicles reflecting boundary conditions were applied instead. This results in a faster clustering since particles which are reflected move towards the center of the simulation box. The reflecting boundary conditions are implemented in the following way: first it is checked whether the new position \mathbf{r}_i is within the open interval $(0.5\sigma, L - 0.5\sigma)$. If $x_i < 0.5\sigma$ the reflected position is $x'_i = -x_i + \sigma$ and if $x_i > L - 0.5\sigma$ the reflected position is $x'_i = 2L - x_i - \sigma$ and the new velocity is $v'_{x_i} = -v_{x_i}$. These boundary conditions are correspondingly applied to the y - and z -direction. A graphical depiction of the reflecting boundary conditions can be found in Fig. 3.3 (b).

3.4 Search Algorithms

The force calculation takes place in the inner most loop. Therefore, with the assumption that each particle i interacts with all particles $j \neq i$, $N(N - 1)$ force calculations are performed, see Fig. 3.4 (a). The following description of improving computational efficiency with respect to force calculation follows Ref. [34]. However, since all forces are truncated at a certain radius r_{max} most of the forces are zero anyway. Hence, a calculation of all $N(N - 1)$ interactions is computationally inefficient. In order to gain computational efficiency the simulation box is divided into subcells of length r_{max} . Only particles interact with each other which are either in the same subcell or in neighbouring cells, see Fig. 3.4 (b),

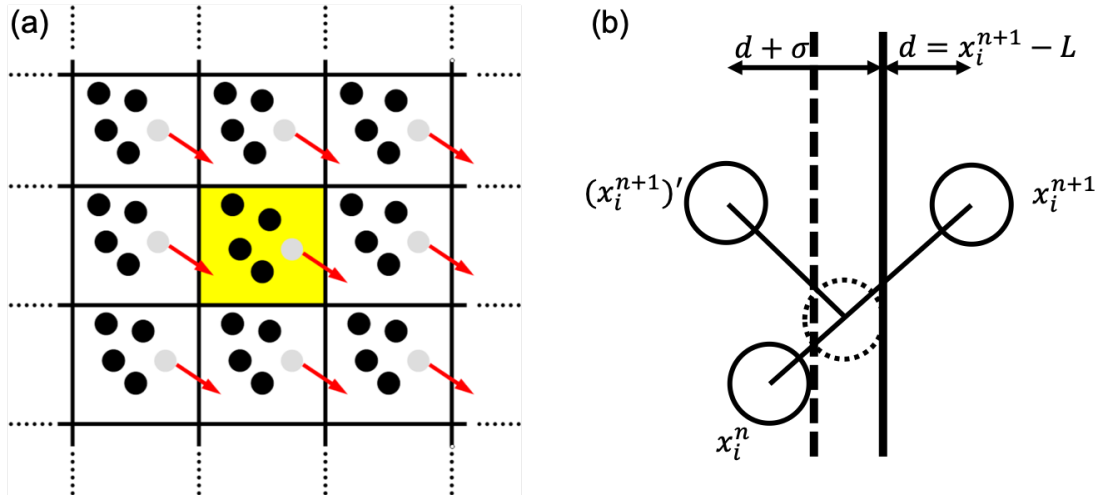


Figure 3.3: (a) Schematic depiction of periodic boundary conditions in two dimensions. If one particle leaves the simulation box on one side, one of its images enters the box on the opposite side. The figure is taken from Ref. [34]. (b) Graphical depiction of the reflecting boundary conditions which were applied.

hence, the force acting on particle i is

$$\mathbf{F}_i = \sum_{\substack{\text{cell } m \\ m \in \Omega(n)}} \sum_{\substack{j \in \text{all particles in cell } m \\ i \neq j}} \mathbf{F}_{ij}, \quad (3.14)$$

where $\Omega(n)$ denotes all neighboring cells of cell n as well as the cell itself. Although this reduces force calculations significantly only about $\frac{4\pi}{81} \approx \frac{1}{6}$ are interactions with non-zero contribution. Further improvement is introduced by Verlet lists [30]. A list is created which only contains particles $r_{max} + r_{skin} = |\mathbf{r}|$, see Fig. 3.4 (c). Hence, only force calculations of particles within this list are calculated. The additional radius r_{skin} is introduced to include also particles in the list which potentially interact in the next few time steps. On the one hand this raises the computational effort but on the other hand the list is valid for several time steps, typically between 5 to 15, depending on size of r_{skin} . Using such Verlet lists reduces the computational effort from $O(N^2)$ to $O(N)$. The simulations performed in this work used Verlet list with a $r_{skin} = 0.4$ and subcells of size $r_{max} = r_{cut} + h_c$.

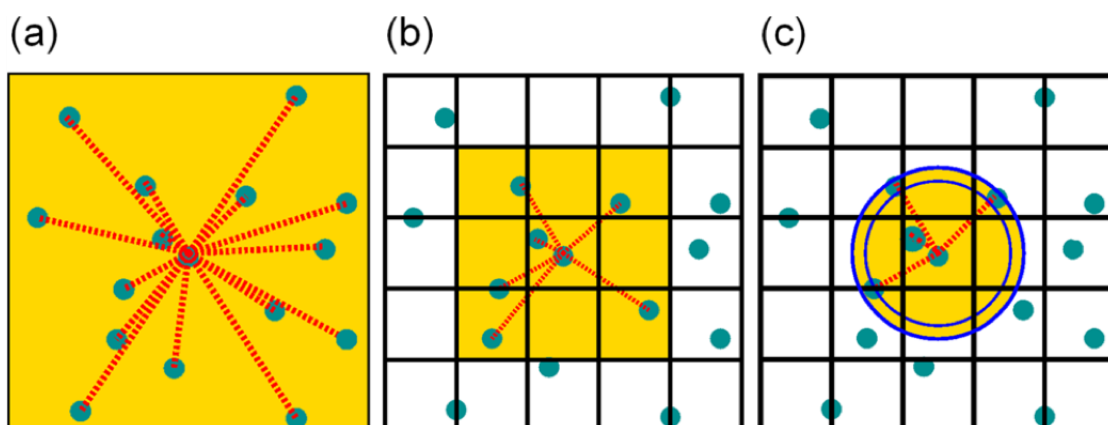


Figure 3.4: Force calculation with Verlet lists: (a) Each particle interact with each other what is not computationally preferable. (b) Division into subcells: Only forces between particles in the subcell and neighbouring cells are calculated. (c) Verlet lists: Only froces between particles with a distance $|\mathbf{r}| < r_{max} + r_{skin}$ are calculated. The figure is taken form Ref. [34].

3.5 Limitations

Despite the MD technique has some unique advantages, especially the insight into the dynamic behaviour of systems, it has its limitations. In the following list some of the most important limitations are discussed [26].

- In order to simulate bulk properties often **artificial boundary conditions** are introduced. The usage of a too small simulation box can cause artificial spatial correlations in too small systems.
- Most of the potentials, described in Sec. 2.3 are **cut off** at a certain distance to improve computational efficiency. Therefore, **long range** interactions such as van der Waals interactions are not taken into account with arbitrary precision.
- Although certain quantum mechanical interactions are taken into account implicitly, e.g. Pauli repulsion in the LJ-(6-12) potential, the particles move according to **classical Newtonian mechanics**. Hence, certain quantum mechanical effects, such as chemical reactions where covalent bonds break or form cannot be simulated.
- Computational power increased enormously during the past decades. However, MD simulations on single CPUs are still restricted to a few hundreds

of thousands of particles and to a few microseconds. Hence, MD simulations are restricted with respect to the **time and length scale**.

4. Measurements

Despite a great deal of information visual inspection gains, it is important to quantify the results of simulations. Several analyzing methods were applied to different systems depending on the quantity which was of most interest. Quantifying only lipid and hybrid systems is based on the radial distribution function (RDF). In this work, systems regarding the interaction between amphiphilic copolymers and vesicles is referred to as *hybrid systems*. Several other interesting system specific quantities were also evaluated for hybrid systems such as the radius of gyration of parts of the polymers. The numerical evaluation of pure amphiphilic copolymer systems required a cluster recognition algorithm since several types of clustering were observed. With the analyzing methods presented in this section, several interesting results could be observed which are presented in Sec. 5.

4.1 Radial Distribution Function

The RDF describes how the density of a systems varies as a function of distance from the center of mass (CM):

$$RDF(\delta r) = \frac{3}{4\pi\delta r^3}n(\delta r), \quad (4.1)$$

where $n(\delta r)$ is the number of monomers in a discrete shell of a sphere of width δr . The center of this sphere is given by the CM which is calculated in the following way:

$$\mathbf{R}_{CM} = \frac{1}{N} \sum_{i=1}^N \mathbf{r}_i. \quad (4.2)$$

Hence, the RDF is a Gaussian-shaped curve for hollow vesicles, see Sec. 5.1.

4.2 Cluster Recognition

For the evaluation of the clusters observed in the study, where we investigated a gel network of amphiphilic copolymers, see Sec. 5.2, two different methods were used. There are a lot of clustering algorithms available such as k -means [35], hierarchical clustering methods [36, 37, 38] or density based methods. The difficulty was to find a cluster recognition algorithm which detects two connected clusters as two separate clusters and the bridge inbetween as noise, see Fig. 4.1 (a). In the first method, the simulation space was subdivided into subcells which were, depending on the density of the surrounding cells, either full or empty [39]. The density of each cell was calculated as

$$\rho_{cell}(\mathbf{k}) = \frac{N_{cell}(\mathbf{k})}{V_{cell}(\mathbf{k})}, \quad (4.3)$$

where $N_{cell}(\mathbf{k})$ was the number of particles and $V_{cell}(\mathbf{k})$ was the volume of the k^{th} cell. Then a weighted density of each cell over the surrounding cells was calculated defined as

$$\bar{\rho}_{cell}(\mathbf{k}) = \frac{1}{35} \left(9\rho_{cell}(\mathbf{k}) + \sum_{\mathbf{k}} \rho_{cell}(\mathbf{k} + \delta\mathbf{k}) \right), \quad (4.4)$$

where the sum was performed over the 26 surrounding neighboring cells. For the boxsize the cut-off radius $r_c = \sqrt[6]{2}$ of the WCA potential was chosen. A cell was defined as filled or empty if $\bar{\rho}_{cell}(\vec{k}) > \rho_{min}$ or $\bar{\rho}_{cell}(\vec{k}) < \rho_{min}$, respectively. With a value of $\rho_{min} = 0.75$ in all systems no bridges were observed, see Fig. 4.1 (c). Afterwards, in order to recognize the clusters, a Density-Based Spatial Clustering of Applications with Noise (DBSCAN) [40] algorithm was applied. The parameters of this algorithm were chosen in a way that no noise was recognized.

Choosing the parameters of the DBSCAN algorithm in a certain way, this algorithm was able to detect the bridges between the clusters as noise, see Fig. 4.1 (b). The DBSCAN algorithm works in the following way: A fixed radius r around each particle is scanned. If a minimum number of other particles N_{min} is within this range, the particle is assigned to a cluster otherwise it is defined as noise. By choosing $r = 1.2$ and $N_{min} = 3$, only the DBSCAN algorithm was able to detect the bridges as noise. In order to compare the two methods i.e. the cell based method with DBSCAN and DBSCAN only, the number of detected particles was compared. It could be observed that the DBSCAN algorithm was able to correctly assign more particles to a cluster than the cell based variant, see Fig. 4.2. The latter detected less particles due to the fact that particles at the outer

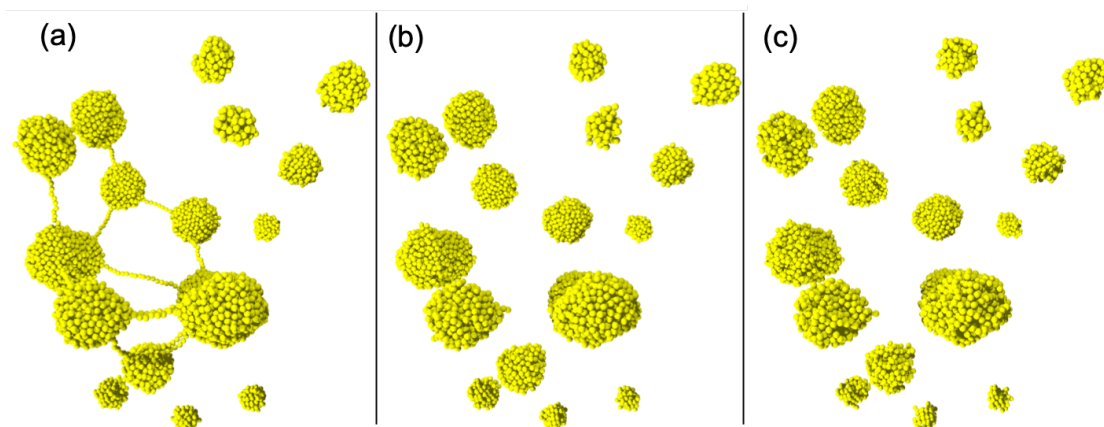


Figure 4.1: Cluster recognition methods: (a) Original system showing only hydrophobic particles with connected clusters. (b) Cluster recognized with the DBSCAN method. (c) Cluster recognized with the cell based method. Here, the hydrophobic particles of the polymer are presented in yellow. In all other snapshots they are presented in blue.

edge of the clusters have a too low density in the surrounding computational cells so that the cells were marked as empty. One disadvantage the DBSCAN method turned out to be the fact that this algorithm false detects many small clusters at the beginning of the simulation. However, the advantage of the DBSCAN algorithm was that it was able to detect more particles in the clustered state. Therefore, the following evaluations of cluster formation, as shown in Sec. 5.2, were performed with this algorithm.

4.3 Penetration Rate

Measuring the penetration of polymers into the membrane was based on the RDF of the lipids. If the lipids formed a vesicle, the RDF showed a Gaussian-shaped peak, whose position on the x-axis showed the radius of the vesicle and its width indicated the thickness of the membrane. Detecting penetrated polymers worked in the following way: First, the standard deviation of the RDF was calculated. Then the RDF of the polymers was calculated with respect to the center of mass of the lipids. If one monomer was below the threshold of the standard deviation of the Gaussian-shaped peak, a polymer was defined as penetrated, see Fig. 4.3. The main disadvantage of this evaluation procedure was that it works only for perfectly shaped vesicles due to the fact that the RDF

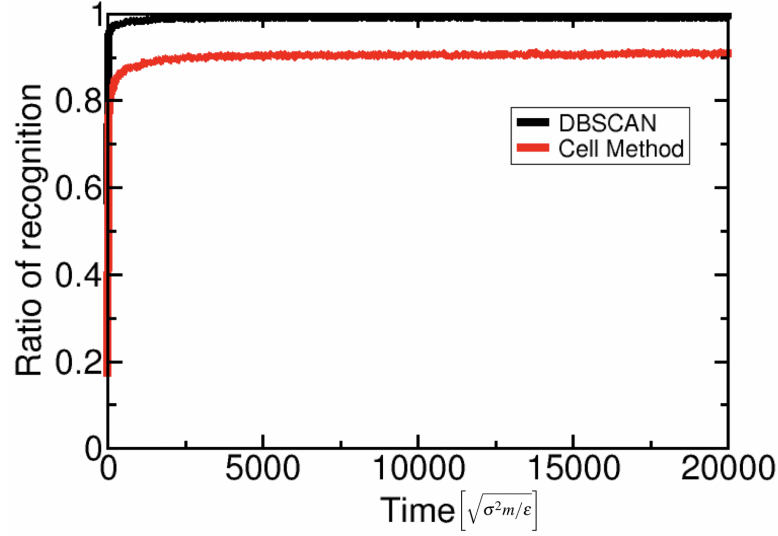


Figure 4.2: Ratio of detected particles with the different cluster algorithms: cell based method and DBSCAN.

had to be Gaussian-shaped. However, since the interaction of polymers was evaluated only for perfectly shaped vesicles this procedure worked very well. Different other quantities were evaluated depending on the topology of the copolymers. In hybrid systems containing amphiphilic star polymers not only the penetration rate of the molecules was calculated but also the penetration rate of the arms. For systems including the amphiphilic bottle brush copolymer with a hydrophobic backbone and hydrophilic arms, the mean squared radius of gyration and the end to end distance of the arms was calculated. The radius of gyration of one arm was

$$\langle R_g^2 \rangle = \frac{1}{N} \sum_{i=1}^{N_{arm}^{length}} \langle (\mathbf{r}_i - \mathbf{R}_{CM})^2 \rangle, \quad (4.5)$$

and its mean squared end to end distance was defined as

$$\langle R_e^2 \rangle^2 = \langle (\mathbf{r}_{N_{arm}} - \mathbf{r}_1)^2 \rangle. \quad (4.6)$$

This calculation was performed separately for penetrated and non-penetrated molecules and allowed to compare the spacial extension of the arms.

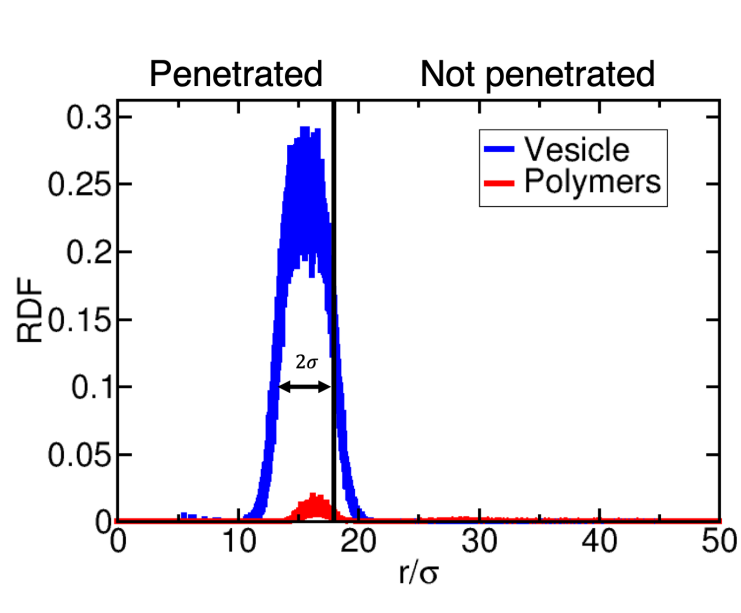


Figure 4.3: Determination of the penetration rate. If one hydrophobic particle of an arm of a star or a backbone of a bottle brush polymer type A is below the threshold, the polymer or the arm is considered to have penetrated the membrane.

5. Results and Discussion

In this chapter, three different studies, performed in this work, are presented. In a first part, the search for optimal parameters which lead to hollow spherical vesicles is presented. Moreover, findings of other interesting self-assembled structures such as vesicle-in-vesicle are shown. Before studying the interaction of the vesicles with amphiphilic polymers, in a second part, a study is presented where the self-assembly of amphiphilic copolymers was investigated. The different polymer topologies showed very different cluster formation. Especially the bottle brush polymer with a hydrophobic backbone and hydrophilic arms showed interesting self-assembled structures such as vesicles, membranes and connected clusters. The last part presents the interaction of vesicles with amphiphilic copolymers. Penetration of the hydrophobic parts of the polymers was observed and different penetration rates were determined, which strongly depended on the polymer topology.

5.1 Vesicle Formation

Studying the interaction of amphiphilic copolymers with vesicles gains more information than the study of flat membranes, since vesicles are closer related to biological systems in nature. However, the self-assembled formation of vesicles is more complex than of flat membranes. This complexity arises from the enormous parameter space and the fact that vesicles occur only in a narrow parameter range. Therefore, in this section, a parameter study regarding the formation of vesicles is presented. All parameters which were tested are shown in Table 5.1. For each combination of parameters only one simulation of a single system was performed and equilibrated over 1.000.000 integration steps. Although there are no statistical results over an ensemble of systems, several well distinguishable forms of self-assembly could be observed.

For $T = 1.5$ in combination with $h_c = 1.5$ no clustering of the lipids was observed. This is in agreement with Ref. [14] where the same software with the same parameter combination showed no cluster formation either. This can

Table 5.1: Parameters which were tested for the vesicle formation: temperature T , hydrophobic attraction h_c , system size N_{lipid} , density ρ and the bending constant κ_{BEND} .

T	1.0	1.5		
h_c	1.5	1.8		
N_{lipid}	1000	5000	10000	
ρ	0.05	0.1	0.15	0.2
κ_{BEND}	0	1	2	10

be explained with a strong random fluctuation of the particles due to the temperature and the low range of hydrophobic attraction. For all other parameter combinations, phase diagrams according to visual expectation were created. The higher the number of lipids in the simulation, the more different forms of self-assembling could be differentiated.

For systems containing 1000 lipids, membranes and vesicles were observed, see Fig. 5.1. At temperature $T = 1.0$ and a hydrophobic attraction range of $h_c = 1.8$, membrane clustering was observed for a bending constant $\kappa_{BEND} \geq 1.0$ and density $\rho \leq 0.1$. For the remaining parameter range at the same temperature and hydrophobic attraction range, vesicular clustering was observed. Similar results can be found for other combinations of temperature and hydrophobic range, see Appendix Fig. A.1 and A.2. The figures in the appendix sometimes show a structure referred to as *undefined clustering*. In those cases a cluster formation could be observed but it was not well distinguishable.

For larger systems ($N_{lipid} = 5000$ and $N_{lipid} = 10000$), more different forms of self-assembly were identified. Besides membrane and vesicle formation, membrane-in-vesicle, vesicle-in-vesicle and vesicular clustering was observed. The latter is referred to as the formation of several, smaller vesicles. Figure 5.2 shows the phase diagram of a system with $N_{lipid} = 5000$ at temperature of $T = 1.0$ and a hydrophobic attraction range of $h_c = 1.8$. At low density $\rho \leq 0.1$ and $\kappa_{BEND} < 10$, either vesicular clustering or vesicles were found. At densities $\rho \geq 0.15$ always one large vesicle was found which was hollow at $\kappa_{BEND} = 0$, or enclosed a membrane or another vesicle at higher bending constants. Further results of other combinations of the temperature T and hydrophobic h_c range can be found in the Appendix in Fig. A.3 and A.4.

The formation of hollow vesicles with a size of $N_{lipid} = 10000$ was observed only at temperature $T = 1.0$ and a hydrophobic range of $h_c = 1.8$, see Fig. 5.3. Similar to the systems with $N_{lipid} = 5000$, membranes, vesicular clustering or hollow vesicles could be observed for densities $\rho \leq 0.1$. Systems with higher

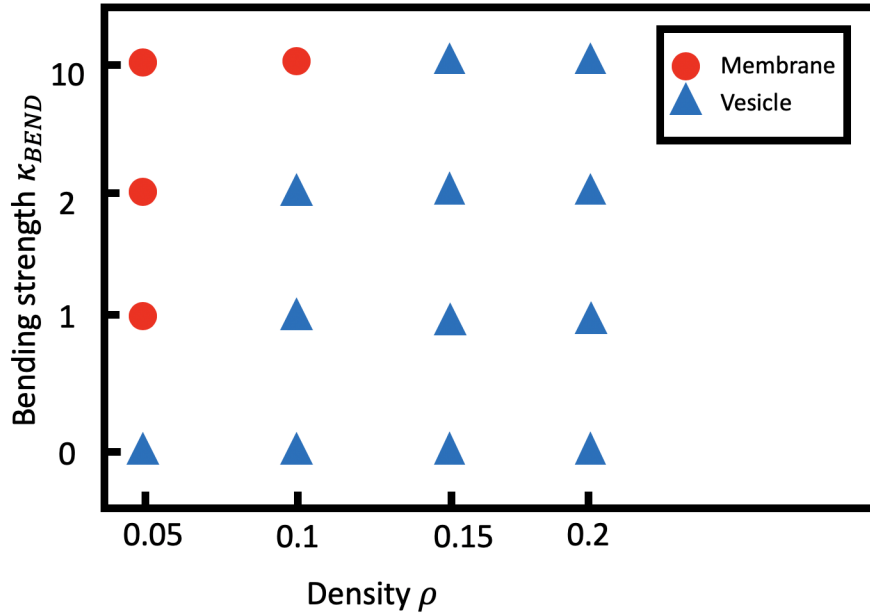


Figure 5.1: Phase diagram of the bending strength κ_{BEND} and density ρ at fixed temperature $T = 1.0$ and hydrophobic range $h_c = 1.8$ of a system with $N_{lipid} = 1000$ lipids.

densities showed vesicles enclosing vesicles or membranes. More results of other combinations of temperature T and hydrophobic attraction range h_c and the system size of $N_{lipid} = 10000$ can be found in Appendix Fig. A.5 and A.6. In general, formation of hollow vesicles was found in a narrower parameter range the larger the system size was.

In order to quantify the results observed by visual inspection, the radial density function (RDF) was evaluated for the different forms of self-assembly. Figure 5.4 shows the RDF of vesicles with a different number of lipids ($N_{lipid} = 1000, 5000$ and 10000). Corresponding snapshots are shown in Fig. 5.7. As expected, the RDF shows a Gaussian-like shape, since no particles are inside the vesicle and none outside. However, the largest system (black line) shows a kink at the outer side of the line. This can be explained by a membrane flake which is close to the vesicle outside of it which can be seen by visual inspection, see Fig 5.7 (b). The position of the peak on the x-axis determines the radius of the vesicle and its width determines the thickness of the membrane. The larger the number of lipids involved in forming a vesicle is, the larger is the radius of the vesicle. The radius of the vesicles tends to increase linearly with the system size. The thickness of the vesicle membrane is independent of the system size,

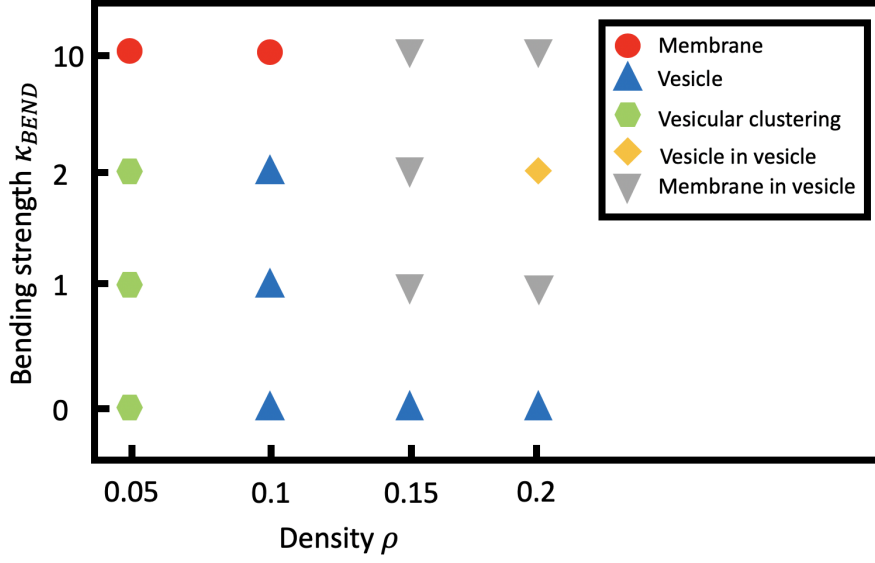


Figure 5.2: Phase diagram of the bending strength κ_{BEND} and density ρ at fixed temperature $T = 1.0$ and hydrophobic range $h_c = 1.8$ of a system with $N_{lipid} = 5000$ lipids.

because it depends on the length of the lipids rather than on the number of lipids.

Not only vesicular clustering could be quantified by the RDF but also other forms of clustering such as vesicle-in-vesicle, membrane-in-vesicle or membrane formation, see Fig. 5.5. Corresponding snapshots can be found in Fig. 5.6. The vesicle in vesicle formation shows two very distinct peaks. Hence, the two vesicles are completely separated. The membrane inside the vesicle shows also two peaks: one very close to the center of mass and one at the same position as the other vesicles. The first peak shows the membrane inside the vesicle whereas the second peak is due to the vesicle itself. Membrane flakes show a broad peak extended over the whole x -axis. Evaluating the same types of clustering of a system of size of $N_{lipid} = 5000$ shows that the outer vesicle in both cases, with a membrane and another vesicle inside, as well as the hollow vesicle, show exactly the same radius, see Appendix Fig. A.7. Besides the vesicle formation, the vesicle-in-vesicle self-assembly is the most interesting result since the double membrane structure occurs in cell compartments such as in mitochondria [41].

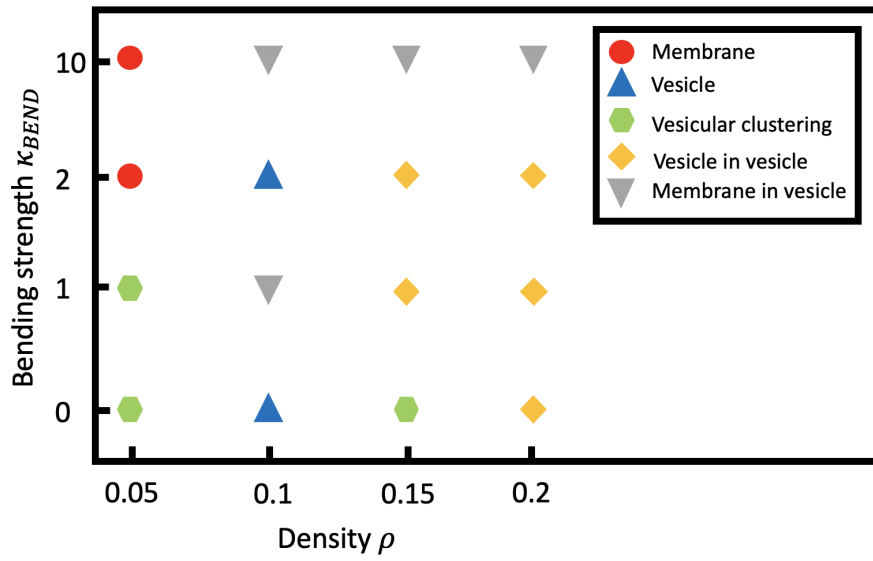


Figure 5.3: Phase diagram of the bending strength κ_{BEND} and density ρ at fixed temperature $T = 1.0$ and hydrophobic range $h_c = 1.8$ of a system with $N_{lipid} = 10000$ lipids.

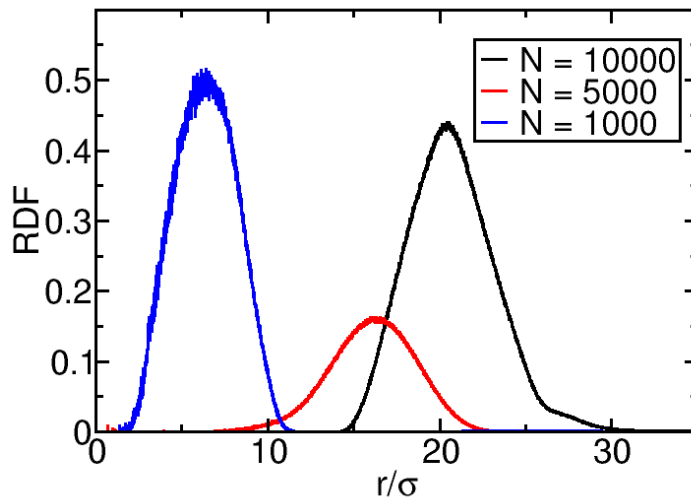


Figure 5.4: Radial density function of vesicles formed with a parameter set of $T = 1.0$, $h_c = 1.8$, $\rho = 0.1$ and $\kappa_{BEND} = 2$.

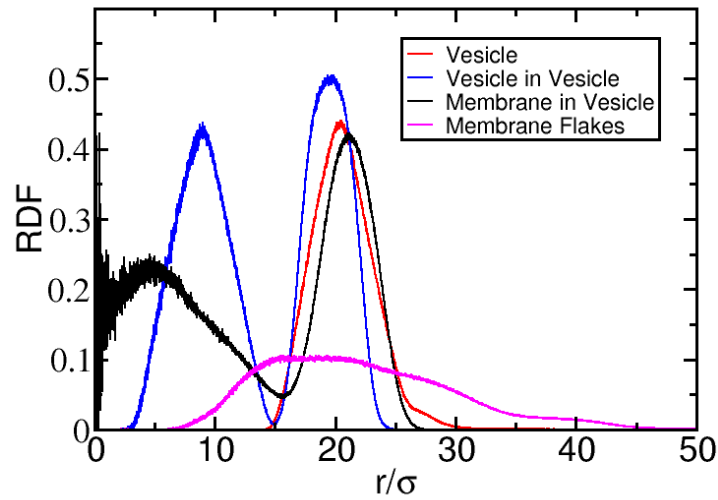


Figure 5.5: Radial density function of different forms of clustering which were observed of a system with $N_{lipid} = 10000$.

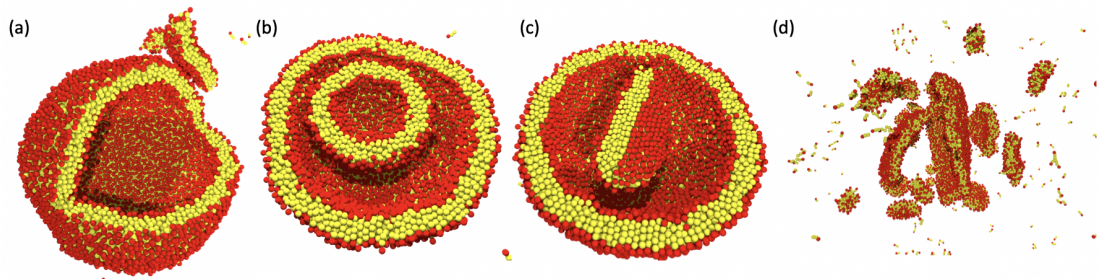


Figure 5.6: Snapshots of different forms of clustering of a vesicle with $N_{lipid} = 10000$: (a) vesicle, (b) vesicle in vesicle, (c) membrane in vesicle and (d) membrane flakes. The hydrophobic particles are presented in yellow and the hydrophilic heads are red colored. Parts of the vesicles are made transparent in order to provide an inside view.

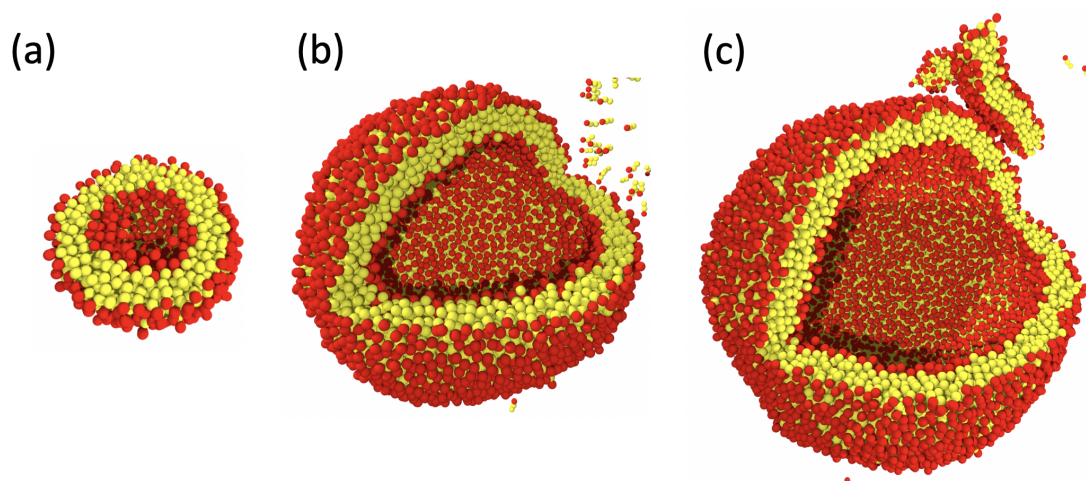


Figure 5.7: Snapshots of vesicles with different size: (a) $N_{lipid} = 1000$, (b) $N_{lipid} = 5000$ and (c) $N_{lipid} = 10000$. The hydrophobic particles are represented in yellow and the hydrophilic heads are in red. Parts of the vesicles are made transparent in order to show the hollow space inside.

5.2 Amphiphilic Copolymers

Before studying the interaction of vesicles with amphiphilic copolymers, first the clustering behaviour of large amphiphilic copolymer networks was investigated. Each tested system was composed of 100 polymers. The polymers can be divided into three different topologies: Stars with a hydrophilic core and hydrophobic arm ends, bottle brush polymers with a hydrophobic backbone and hydrophilic arms and bottle brushes which were partwise hydrophobic, see Sec. 2.1. For all topologies, several parameter sets were simulated and each simulation ran for 2.000.000 integration steps. Due to the fact that the parameter set was too large to evaluate *all* systems numerically, only those systems were evaluated which showed vesicle formation in the study of the self-assembly of lipids, see Sec. 5.1. Hence, temperature $T = 1.0$, a density of $\rho = 0.1$ and a hydrophobic attraction of $h_c = 1.8$ were chosen for a detailed numerical evaluation. Afterwards, the cluster formation was evaluated with the clustering algorithm described in Sec.4.2. Two different aspects are covered with this evaluation. On the one hand, we present in the following section static evaluations which give information about the clustered state; on the other hand, the mean squared radius of gyration of all clusters over time yields information about the dynamics of cluster formation.

Star Polymers

The parameter space which was simulated for this polymer type is shown in Table 5.3. The parameters which were evaluated numerically are presented in bold. The length of the arms of the stars was set constant to $N_{arm}^{length} = 30$.

Table 5.2: Parameters which were tested for the cluster formation: temperature T , hydrophobic attraction h_c , hydrophobicity $N_{hydrophobic}$, functionality f and density ρ .

T	1.0	1.5		
h_c	1.5	1.8		
$N_{hydrophobic}$	4	10		
f	4	9	16	
ρ	0.05	0.1	0.15	0.2

The evaluation of the mean squared radius of gyration of the different clusters showed that the larger the hydrophobic part $N_{hydrophobic}$ was, the larger but fewer clusters emerged, see Fig. 5.9. This behaviour can be explained by the fact that for a larger hydrophobic part the probability is larger to form a cluster with other hydrophobic particles. This effect can also be seen by visual inspection as shown in Fig. 5.8. Stars with higher functionality f also show more clusters but with similar size compared to their counterparts with lower functionality. The explanation for this observation is the increased steric effects in the center of the star with increased functionality f . Hence, the higher the functionality is, the harder it is for the arms to bend in one direction, and therefore the harder the formation of large clusters is; despite the system containing more hydrophobic particles. This effect should be enhanced the shorter the arms are and should vanish with longer arms.

The observation described above could also be validated with the pair correlation function, see Fig 5.10. Star polymers with a larger hydrophobic part $N_{hydrophobic}$ show higher peaks and therefore more structure than those with less hydrophobic particles. Also stars with different functionality f show differences in the pair correlation function. The stars with highest functionality $f = 16$ show more structure than their lower counterparts.

Not only the sizes of the clusters was evaluated but also their shapes. In order to evaluate the shape of a cluster the normalized principal moments or shape factors [42] were evaluated. For spherical clusters the shape factors are $sf_i \approx 1/3$ whereas for rod like clusters $sf_3 = sf_2 = 0$ and $sf_1 = 1$. In Fig. 5.11 the shape factors as well as the radius of gyration of each cluster is shown for a system consisting of stars with a functionality of $f = 16$ and a hydrophobic-

ity of $N_{hydrophobic} = 10$. While smaller clusters show deviations from a spherical shape, larger clusters tend to be almost perfectly spherically shaped. This behaviour was observed for all systems with star polymers.

Figure 5.12 shows the evolution of the cluster formation over time. Each timestep shows the mean squared radius of gyration of all clusters. The size of the clusters over time shows a logarithmic growth. At the beginning, the clusters are emerging fast and then only grow slowly over time.

These results show that the cluster formation depends on the one hand on the functionality f and on the other hand on the number of hydrophobic particles at the end of the arms.

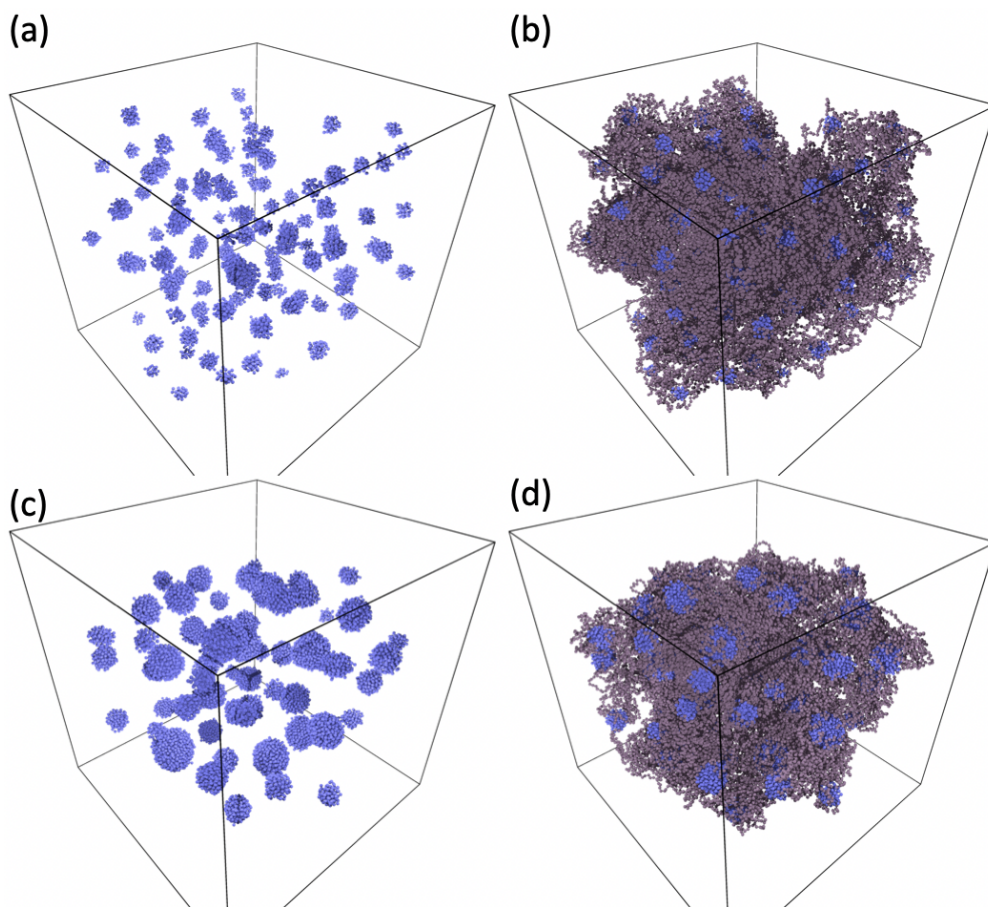


Figure 5.8: Snapshots of an amphiphilic star polymer network with functionality $f = 16$: (a) and (b) hydrophobicity $N_{hydrophobic} = 4$; (c) and (d) hydrophobicity $N_{hydrophobic} = 10$. The hydrophobic particles are presented in blue whereas the hydrophilic particles are grey.

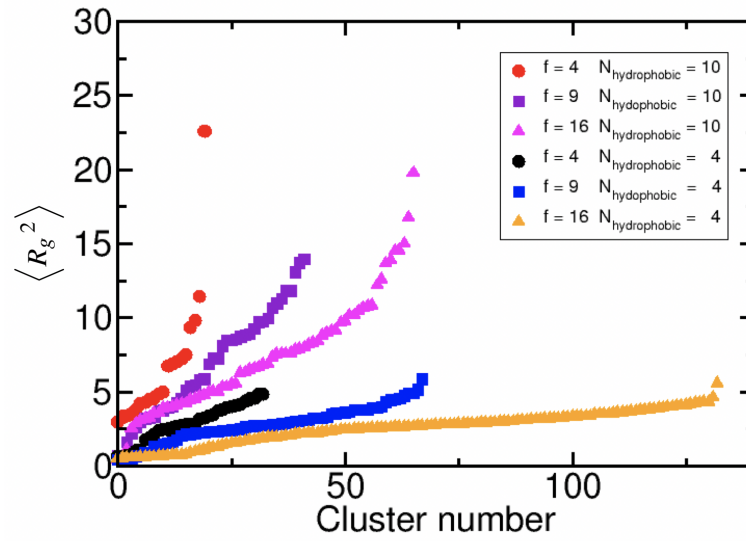


Figure 5.9: Static evaluation of the star polymer networks. The different clusters and their squared radius of gyration.

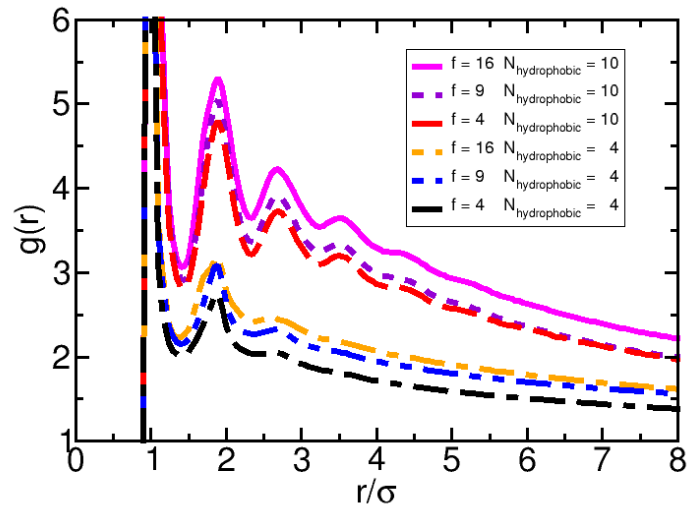


Figure 5.10: Pair correlation function of the star polymer networks.

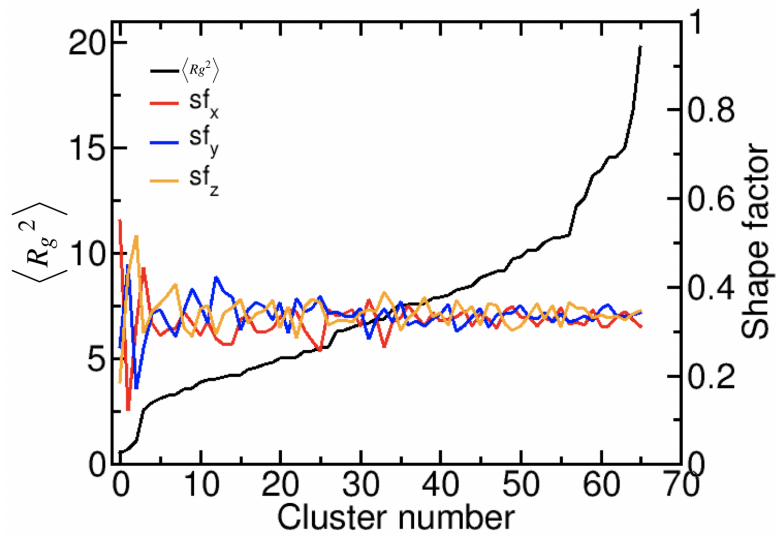


Figure 5.11: Evaluation of the shape factors of the clusters of one star polymer network with a functionality of $f = 16$ and a hydrophobicity of $N_{hydrophobic} = 10$.

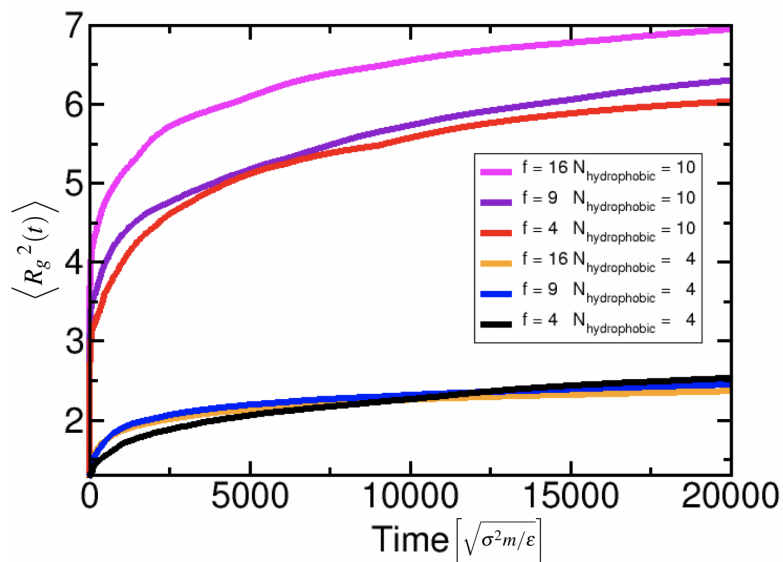


Figure 5.12: Growth of the star polymer network over time.

Bottle Brush Type A

This type of bottle brush polymer showed very different forms self-assembly. Vesicular and membrane-like structures as well as clusters connected through the hydrophobic backbone could be observed, see Fig. 5.13 and 5.17. The self-assembly strongly depended on the polymer topology, especially on the length and number of hydrophilic arms. In Table 5.3 the different parameters are presented and those which were evaluated numerically are bold. The arms were always equally distributed attached to the backbone whose length was set constant to $N_{backbone} = 100$. As elucidated above, due to the large parameter space not all parameter combinations were evaluated numerically.

Table 5.3: Parameters which were tested for the cluster formation: temperature T , hydrophobic attraction h_c , number of arms N_{arms} , arm length N_{arm}^{length} and density ρ .

T	1.0	1.5		
h_c	1.5	1.8		
N_{arms}	10	50		
N_{arm}^{length}	5	30		
ρ	0.05	0.1	0.15	0.2

Like for the star polymers for this polymer network, static as well as evaluations over time were performed. The size of the different clusters depended strongly on the topology of the polymers. While polymers with short arms formed a few, small clusters, those with long arms showed many small clusters, see Fig. 5.14. Also the number of arms influenced the emergence of clusters. Low grafting density, hence only a few arms are attached to the backbone, resulted in larger clusters than high grafting density. This observation can be explained by a shielding effect of the hydrophilic arms. The more arms or the longer they are, the more the hydrophobic backbone is shield from interactions with backbones of other polymers. This observation is also validated by the pair correlation function, see Fig. 5.15. Polymers with low grafting density or short arms show higher and more peaks and therefore more structure than those with high grafting density or long arms.

The evolution of the cluster formation over time showed that the clusters grow much faster in the beginning with bottle brush than with star polymers, see Fig. 5.12 and 5.16.

Vesicular formation was observed at higher densities $\rho > 0.1$ and only for short arms $N_{arm}^{length} = 5$ at low grafting density. In Fig. 5.17 the RDF of a vesicle is presented. The Gaussian-shaped peak and therefore the vesicle is much thicker

than the vesicles formed by lipids due to the fact that the number of hydrophobic particles is much larger. Furthermore, the RDF shows that the space inside the hollow vesicle, is much smaller than in lipid vesicles. A larger space can be expected when simulating either more or shorter amphiphilic polymers. The results presented for this polymer type showed very different forms of self-assembly strongly depending on the individual parameter combinations. Moreover, a shielding effect could be observed caused by the hydrophilic arms.

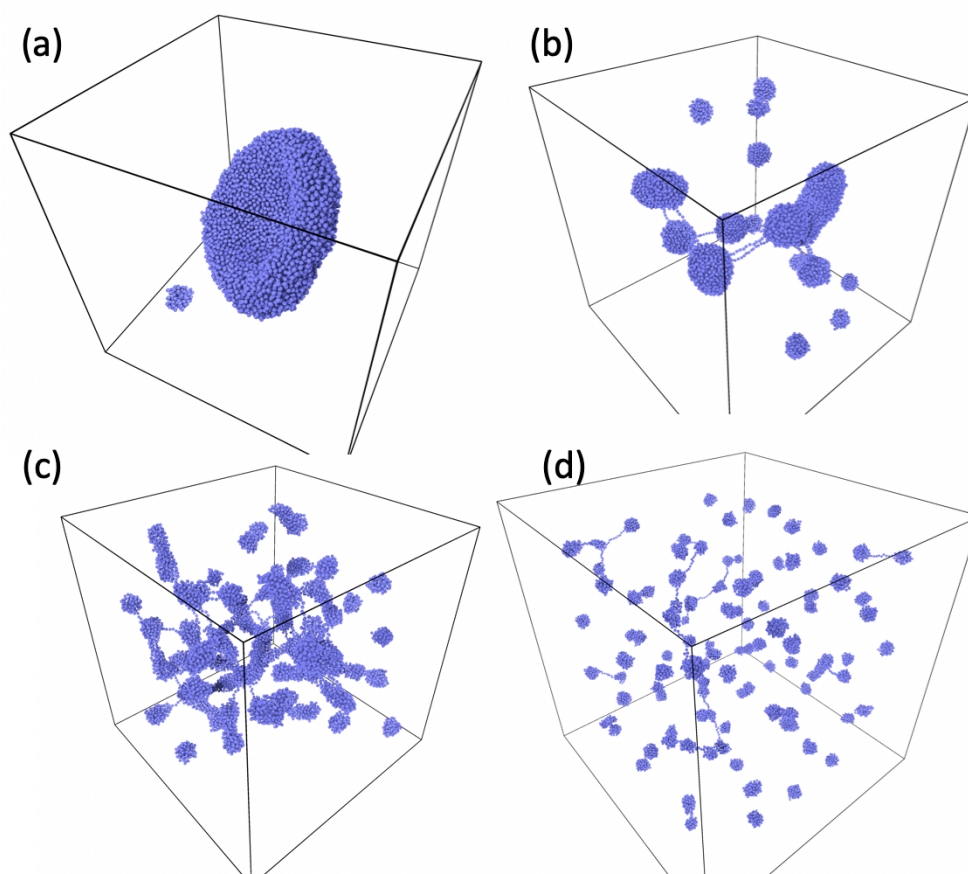


Figure 5.13: Snapshots of the different cluster formations which were evaluated: (a) $N_{arm} = 10$, $N_{arm}^{length} = 5$; (b) $N_{arm} = 10$, $N_{arm}^{length} = 30$; (c) $N_{arm} = 50$, $N_{arm}^{length} = 5$; (d) $N_{arm} = 50$, $N_{arm}^{length} = 30$. The snapshots show the clusters of the hydrophobic part. Corresponding snapshots also including the hydrophilic part can be found in the Appendix in Fig. B.3.

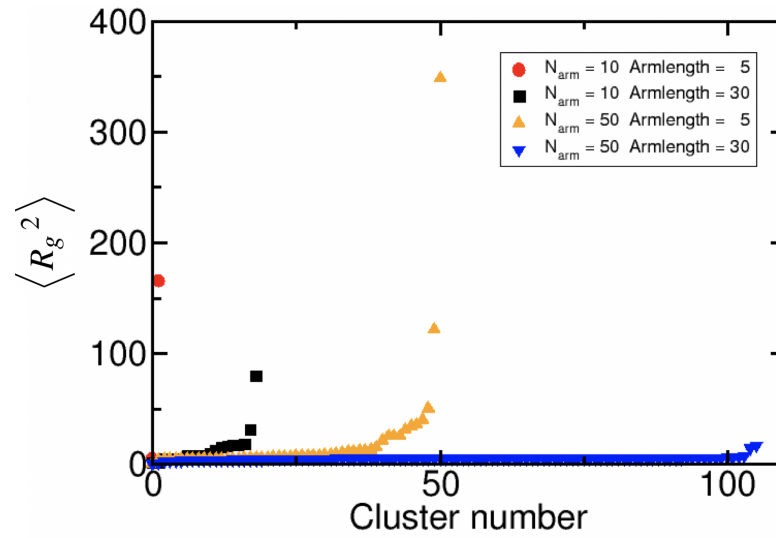


Figure 5.14: Static property of a bottle brush polymer network. The different clusters and their corresponding mean-squared radius of gyration are displayed.

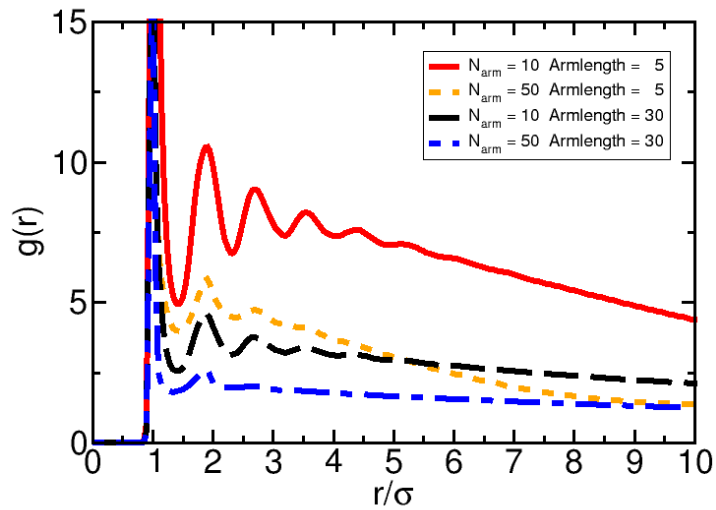


Figure 5.15: Pair correlation function of bottle brush polymer networks.

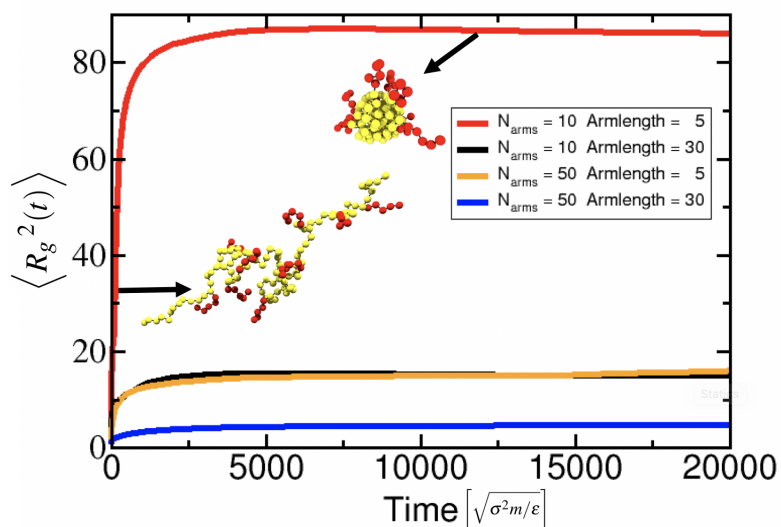


Figure 5.16: Time evolution of a bottle brush polymer network. Time versus the mean-squared radius of gyration of the clusters. The snapshots show one polymer stretched at the beginning of the simulation and another one after cluster formation has started. Hydrophobic parts are presented in yellow color whereas the hydrophobic arms are displayed in red color.

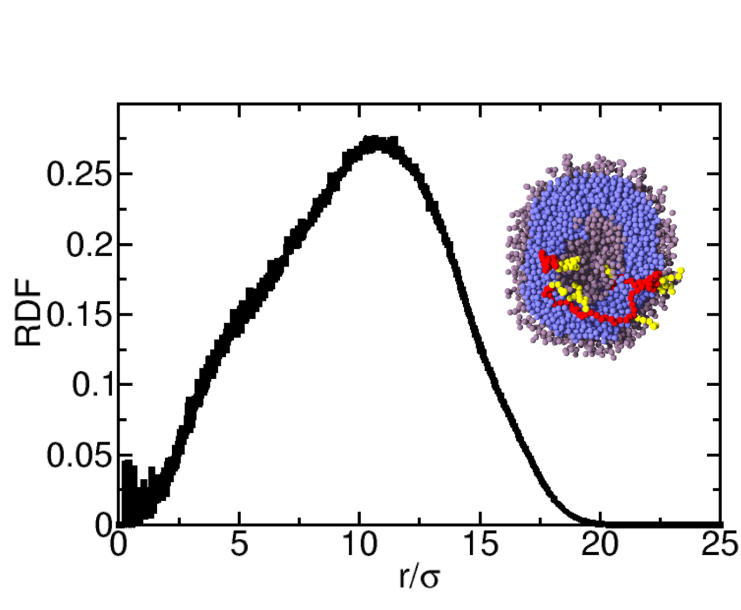


Figure 5.17: RDF of the vesicle formation of polymer type A and a corresponding snapshot. Only a part of the vesicle is presented in order to allow a view inside. In yellow (hydrophilic) and red (hydrophobic), one bottle brush polymer is presented in order to show a possible arrangement inside the vesicle, as observed in our simulations.

Bottle Brush Type B

Simulations of bottle brush polymer type B were performed for three different fractions of hydrophobicity. *Type B1* is referred to a bottle brush polymer where half of the polymer is hydrophobic (backbone and arms) and the other part hydrophilic. For *type B2* and *type B3* the ratio of hydrophobicity is 1/3 and 2/3 respectively. Table 5.4 shows the parameter space which was simulated. Due to the fact that the parameter space was too large in order to evaluate all systems numerically only the values in bold were evaluated numerically.

Table 5.4: Parameters which were tested for the cluster formation: temperature T , hydrophobic attraction h_c , number of arms N_{arms} , arm length N_{arm}^{length} and density ρ .

T	1.0	1.5		
h_c	1.5	1.8		
N_{arms}	10	50		
N_{arm}^{length}	5	30		
Hydrophobic ratio	1/3	1/2	2/3	
ρ	0.05	0.1	0.15	0.2

Despite polymer type B has a similar topology to polymer type A, neither vesicular nor membrane formation was observed by visual inspection. Only connected and well distinct cluster formation was identified.

Polymer type B2 with a hydrophobic ratio of 1/3 shows a similar clustering behaviour as bottle brush type A. Bottle brush polymers with a low grafting density and short arms show a few but rather large clusters whereas high grafting density and long arms emerge many small clusters, see Fig. 5.18. Evaluating the mean squared radius of gyration over time validates the results of the static evaluation. Fast cluster formation at the beginning can be observed, except for the polymers with lowest grafting density $N_{arm} = 10$ and with shortest arms $N_{arm}^{length} = 5$, see Fig 5.19. This topology shows a constant increase of the mean squared radius of gyration with time and therefore a constant increase of the size of the clusters.

A hydrophobic ratio of 1/2 shows a similar cluster formation to the ratio of 1/3. Again, polymers with low grafting density and short arms tend to form fewer but larger clusters, see Fig. 5.20. Comparing the polymers with $N_{arm} = 10$ and $N_{arm}^{length} = 30$ with $N_{arm} = 50$ and $N_{arm}^{length} = 5$, approximately the same number of clusters can be observed. However, the polymer with lower grafting density shows a larger difference in the size of the clusters than those with higher graft-

ing density. The dynamic evaluation shows as well a fast cluster formation at the beginning, where the polymers with low grafting density and short arms show in general a higher radius of gyration which validates the static evaluation, see Fig. 5.21.

The polymer with highest hydrophobic ratio 2/3 shows the most interesting results regarding the number of clusters and its corresponding size. The polymer with the lowest grafting density $N_{arm} = 10$ and shortest arms $N_{arm}^{length} = 5$ as well as the polymer with the highest grafting density $N_{arm} = 50$ and longest arms $N_{arm}^{length} = 30$ show more and smaller clusters than the two other polymer topologies, see Fig. 5.23. However, the mean squared radius of gyration shows the same systematic behaviour as for the other hydrophobic ratios. Polymers with low grafting density and short arms show a higher mean squared radius of gyration than polymers with high grafting density and long arms, see Fig. 5.24.

Comparing the mean squared radius of gyration over time, regarding the different hydrophobic ratios, polymers with higher hydrophobic ratio tend to form larger clusters than polymers with a smaller hydrophobic part, see Appendix B Fig. B.4, B.5 and B.6. The polymer with the highest grafting density $N_{arm} = 50$ and the longest arms $N_{arm}^{length} = 30$ shows an exception in this behaviour. Not the polymer with the highest hydrophobic ratio 2/3 shows the largest radius of gyration but the polymer with a hydrophobic ratio of 1/2, see Fig. B.7.

The results of bottle brush polymer type B are not as systematic as for stars and polymer type A polymers. Nevertheless, higher hydrophobic ratios tend to form larger clusters and a great influence of the grafting density and the arm-length could be observed. Other self-assembly formations such as vesicles and membranes are expected to occur in systems containing shorter polymers with a hydrophobic ration of 2/3, similar to that of lipids [4].

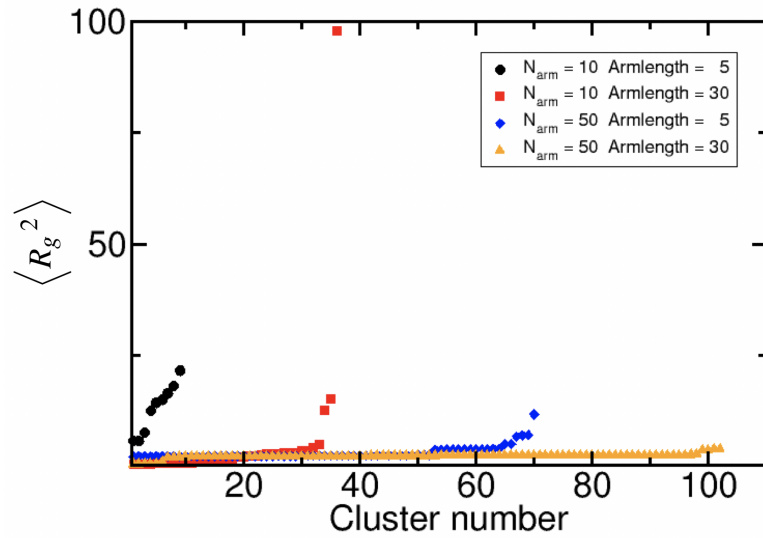


Figure 5.18: Static property of the cluster formation of bottle brush polymers with a hydrophobic ratio of 1/3: The different clusters and their squared radius of gyration.

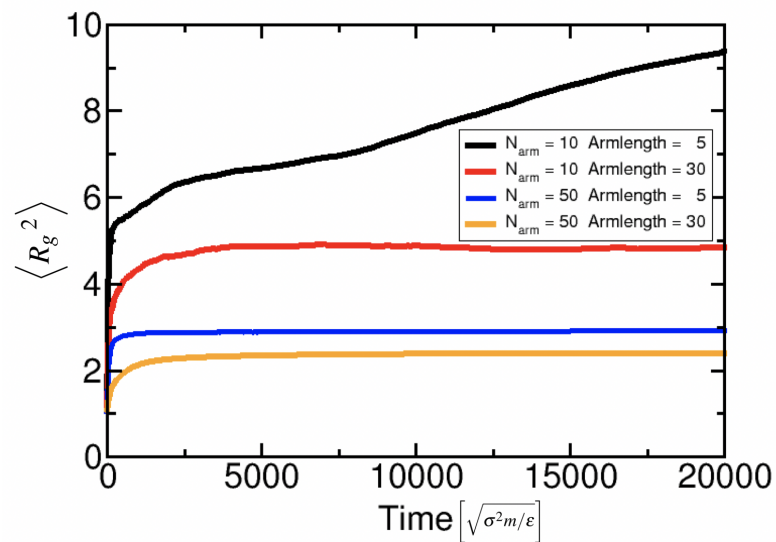


Figure 5.19: Time evolution of bottle brush polymers with a hydrophobic ratio of 1/3: The mean radius of gyration over time.

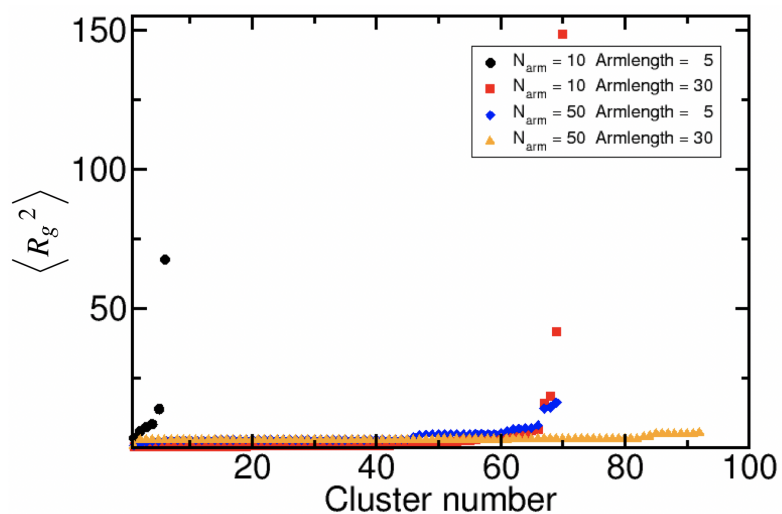


Figure 5.20: Static property of the cluster formation of bottle brush polymers with a hydrophobic ratio of 1/2: The different clusters and their squared radius of gyration.

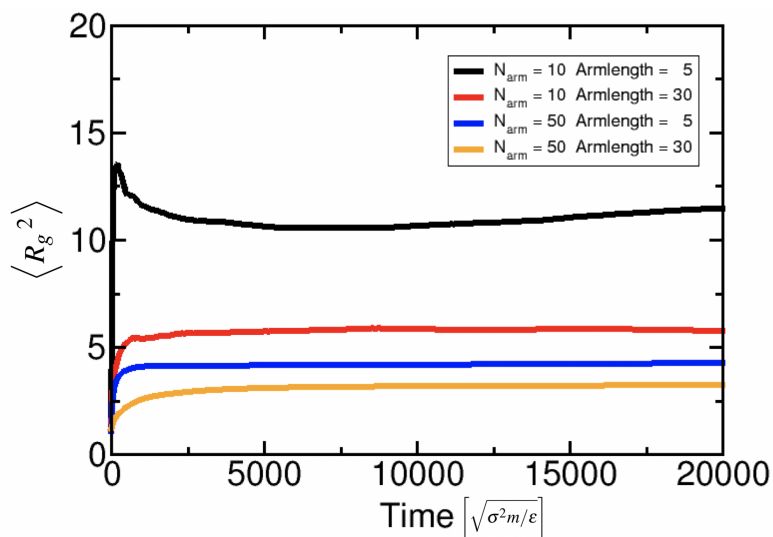


Figure 5.21: Time evolution of bottle brush polymers with a hydrophobic ratio of 1/2: The mean radius of gyration over time.

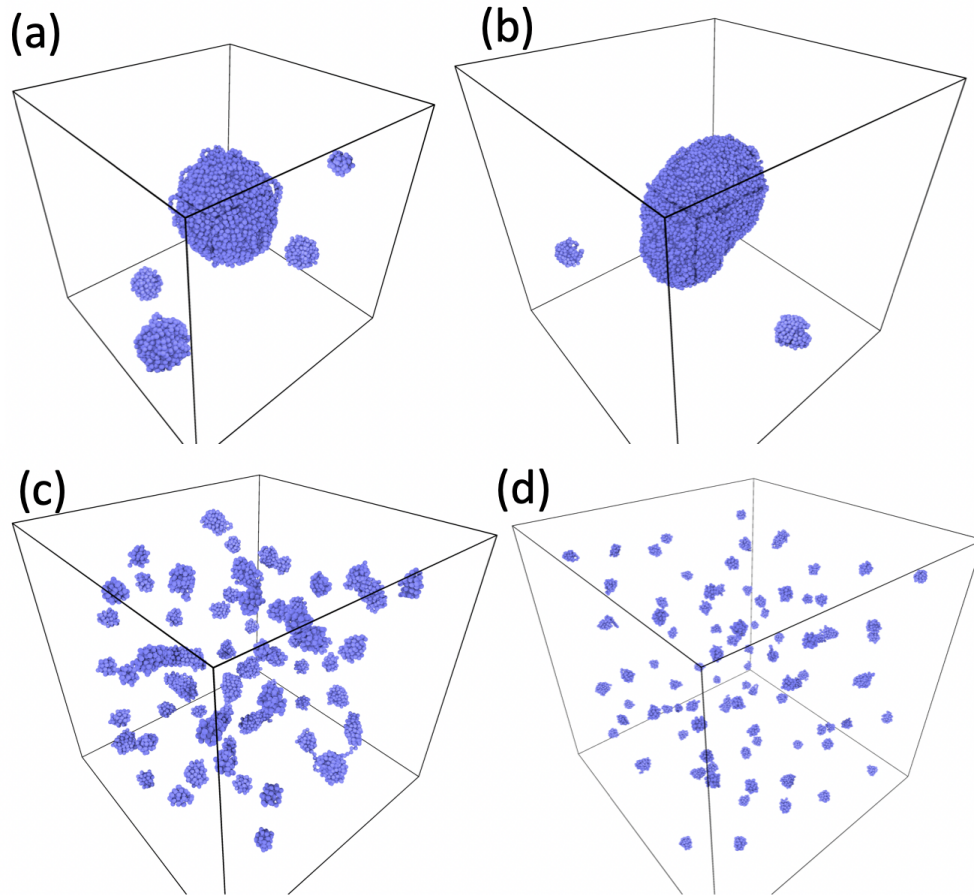


Figure 5.22: Snapshots of bottle brush polymers type B with a hydrophobic ratio of 1/2: (a) $N_{arm} = 10, N_{arm}^{length} = 5$; (b) $N_{arm} = 10, N_{arm}^{length} = 30$, (c) $N_{arm} = 50, N_{arm}^{length} = 5$; (d) $N_{arm} = 50, N_{arm}^{length} = 30$. Presented are only the hydrophobic parts. A figure also including the hydrophilic parts can be found in the Appendix in Fig. B.8.

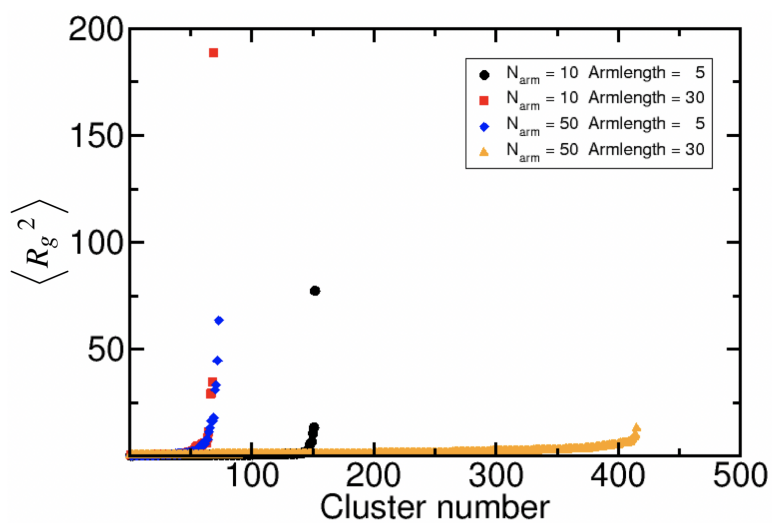


Figure 5.23: Static property of the cluster formation of bottle brush polymers with a hydrophobic ratio of 2/3: The different clusters and their squared radius of gyration.

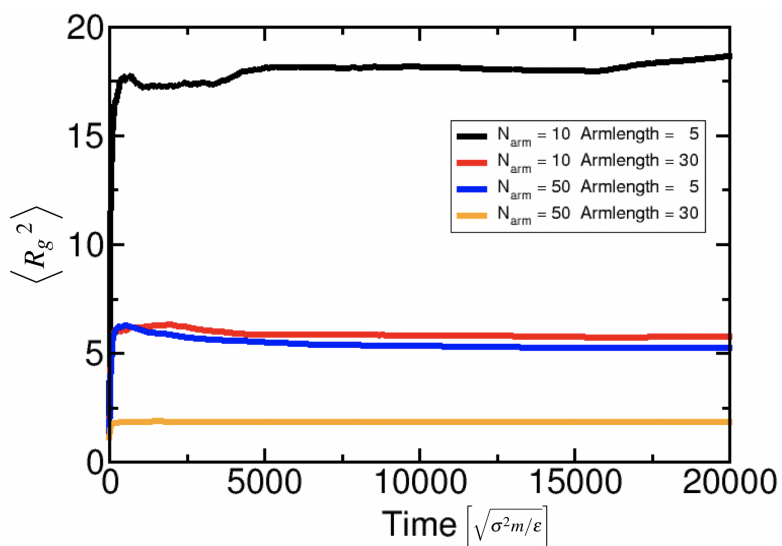


Figure 5.24: Time evolution of bottle brush polymers with a hydrophobic ratio of 2/3: The mean squared radius of gyration over time.

5.3 Interaction of Amphiphilic Copolymers with Vesicles

The interaction of vesicles with amphiphilic copolymers was studied with the parameters of temperature $T = 1.0$, hydrophobic range $h_c = 1.8$ and density $\rho = 0.1$. Three different bending strengths were applied to the lipids, $\kappa = 0.0, 1.0$ and 2.0 . Those parameters showed vesicle formation of a system consisting of 5000 lipids. Only simulations with systems containing 5000 lipids were evaluated since vesicle formation occurred in almost all simulations. Systems consisting of 10000 lipids showed in almost all cases no self-assembly to vesicles and therefore no statistical relevant ensemble could be provided for evaluations. Vesicles consisting of 1000 lipids were proven as too small so that the interaction with amphiphilic copolymers resulted in its destruction. While the lipids included a bending potential so that they are stretched, the amphiphilic copolymers simulated here were fully flexible chains. Interactions of vesicles with amphiphilic star and bottle brush polymers of type A were studied. Each vesicle was surrounded by 10 polymers. This number was tested in advance and it was shown that a lower number of polymers results in too less interaction and a higher number in the destruction of the vesicles. In this section first the results of the interaction of star polymers is provided followed by bottle brush polymers. Both polymer topologies showed that the penetration rate barely depends on the stiffness of the lipids but rather on the polymer topology.

Star Polymers

The amphiphilic star polymers were composed of arms with a length of 30 monomers. The number of hydrophobic particles at the end of each arm was either $N_{hydrophobic} = 4$ or 10 and the functionalities were $f = 4, 9$ and 16 . For each star topology five systems were simulated for 1.000.000 integration steps in the prerun and equilibrated for the same number of integration steps in a productive run where the interaction between the polymers and lipids was turned on. At least three systems showed vesicle formation so that the results presented here show a statistical average of at least three systems. The penetration rate of the arms strongly depends on the functionality of the star polymers, see Fig. 5.25. In general the lower the functionality is, the higher is the penetration rate. An explanation for this observation is that the more arm a star has the higher its density at the center is and the harder it is for the star to fold the arms in one direction. Regarding the number of hydrophobic monomers it can be observed that the penetration rate for less hydrophobic monomers tends to be higher, especially for a functionality of $f = 4$. This behaviour can also be

seen if a bending strength of $\kappa = 1.0$ is applied to the lipids, see Appendix C Fig. C.1. This observation can be explained by the fact that 4 hydrophobic molecules fit exactly into the membrane bilayer whose hydrophobic part consists of 4 monomers too. However, the gap between the two hydrophobic ratios decreases with increasing functionality. If a stiffness is applied to the lipids the difference in the penetration rate for higher functionality $f = 9$ and $f = 16$ vanishes, see Fig. 5.26. Corresponding snapshots of the simulated systems can be found in Fig. 5.27. However, this observation has to be treated with caution due to the fact that the ensemble contains at least only three systems and hence the statistical error of the penetration rate is about ± 0.5 . Therefore, in order to proof a dependency of the penetration rate and the lipid stiffness, ensembles containing more systems should be evaluated. Nevertheless, the results have proven a strong influence of the polymer topology regarding the penetration rate, especially the functionality of the stars.

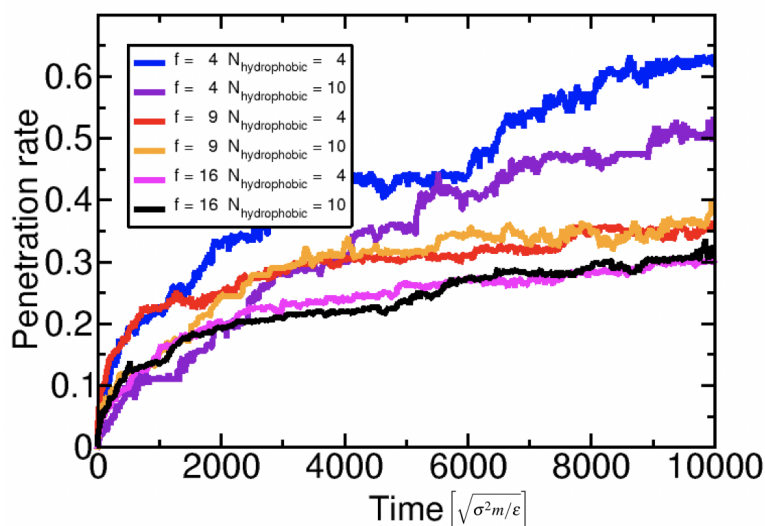


Figure 5.25: Penetration rate of star polymers with different functionality f and hydrophobic ratio $N_{hydrophobic}$. The lipids of the membrane had no bending strength i.e. $\kappa_{BEND} = 0$.

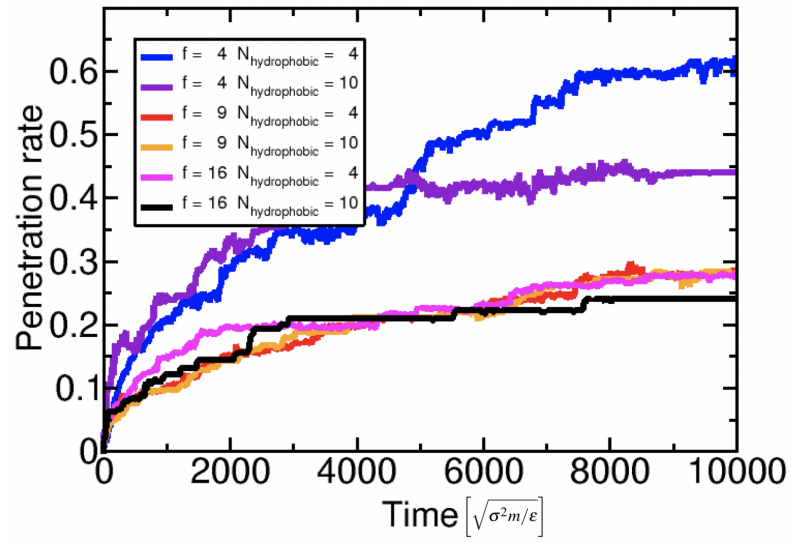


Figure 5.26: Penetration rate of star polymers with different functionality f and hydrophobic ratio $N_{hydrophobic}$. The lipids of the membrane had a bending strength of $\kappa_{BEND} = 2$.

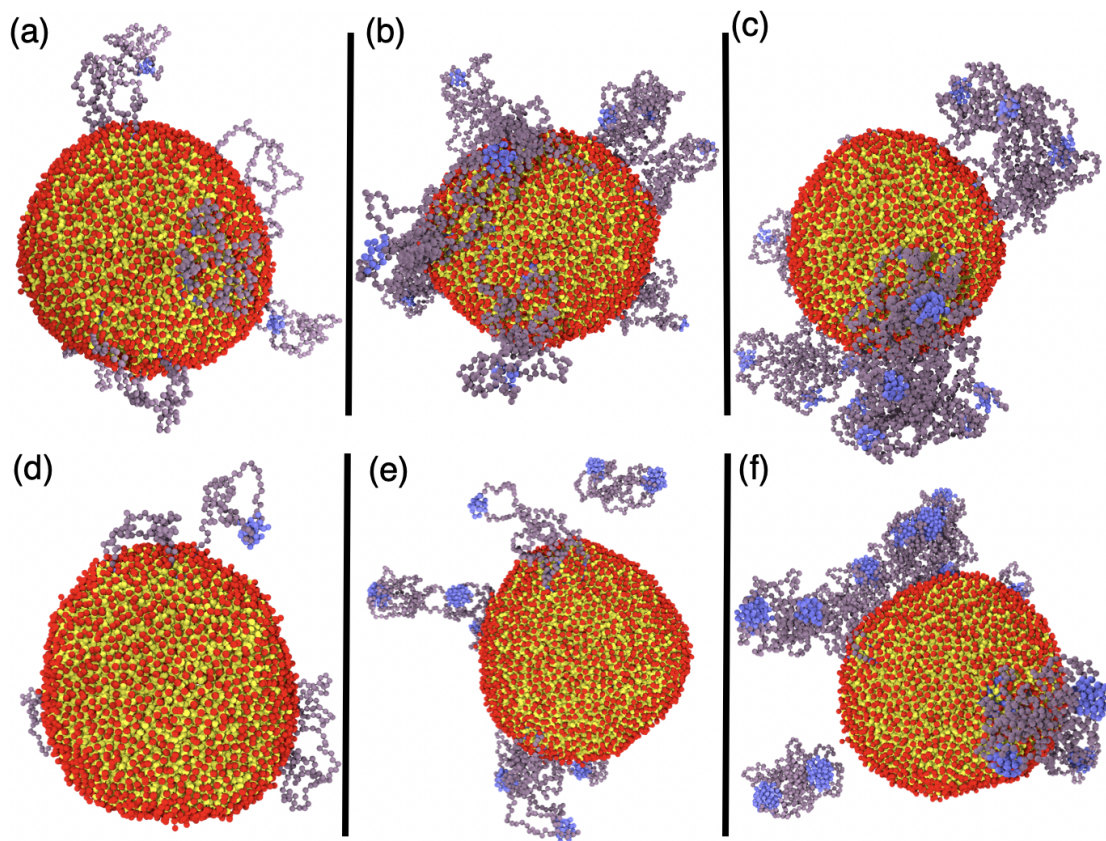


Figure 5.27: Snapshots of the equilibrated systems after 1.000.000 integration steps. Some of the hydrophobic parts of the star polymers have penetrated the vesicle which is formed of 5000 lipids. (a) $f = 4$ and $N_{hydrophobic} = 4$; (b) $f = 4$ and $N_{hydrophobic} = 10$, (c) $f = 9$ and $N_{hydrophobic} = 4$, (d) $f = 9$ and $N_{hydrophobic} = 10$, (e) $f = 16$ and $N_{hydrophobic} = 4$, (f) $f = 16$ and $N_{hydrophobic} = 10$. The lipids are presented in yellow (hydrophobic) and red (hydrophilic) color, respectively, whereas the polymers are presented in blue (hydrophobic) and grey (hydrophilic) color, respectively.

Bottle Brush Type A

Bottle brush polymer type A was composed of a hydrophobic backbone and hydrophilic arms. The length of the backbone was set constant to 100 monomers as well as the number of arms was set to 10 which was the lower grafting density in the polymer network study, see Sec. 5.2. The reason for focusing on polymers with low grafting density was the result of a pre-study which showed no penetration for high grafting density. The length of the arms was $N_{arm}^{length} = 0, 5, 10, 30$ and 50 where an armlength of 0 is a full flexible hydrophobic linear chain which only consists of the backbone. Snapshots of the systems can be found in Fig. 5.33. For each polymer topology an ensemble of ten systems was simulated and at least seven systems showed vesicle formation so that the results presented here show a statistical average of at least seven systems. The prerun which ensured the self-assembly of vesicles ran for 1.000.000 integration steps. The systems ran for 10.000.000 integration steps in the productive run to increase the probability of penetration. In order to check whether the systems were equilibrated the energies examined. If the energy is fluctuating around a mean value, a system was considered to be equilibrated, see Fig. 5.28. The potential energy is decreasing in the prerun of the simulation and after a few thousand timesteps fluctuating around a mean value. During the productive run the potential energy is further decreasing due to the turned on interactions between the lipids and the polymers and is again fluctuating after a few hundred integration steps around a mean value.

The penetration rate of the polymers showed that the longer the hydrophilic arms are the harder it is for the polymer to penetrate the membrane, independent of the lipid stiffness κ , see Fig. 5.29 and 5.30. This observation can be explained by a shielding effect of the hydrophilic arms. The longer they are the harder it is for the hydrophobic backbone to come close enough to the membrane for hydrophobic attraction. Hence, the probability of hydrophobic attraction and therefore penetration decreases with increasing armlength. For arms longer than $N_{arm}^{length} = 30$ this effect saturates i.e. there is barely any difference in the penetration rate of $N_{arm}^{length} = 30$ and $N_{arm}^{length} = 50$. Therefore, it is expected that even longer arms show a similar penetration rate. On the other hand the case where no arms are attached to the polymer and only a hydrophobic linear polymer is interacting with the vesicle, complete penetration of all polymers could not be observed. An explanation for this observation is that the density was relatively small and therefore the box was large so that some polymers at the edge of the box never came close enough to the membrane in order to interact with the vesicle. This effect should vanish running the simulation for even more integration steps so that the polymers at the edge of the box have more

time to get close enough to the vesicle to interact. Moreover, this could also be used as a benchmark of the number of integration steps of further studies. The number of integration steps in the productive run could be defined as the number of integration steps it takes until all polymers with armlength 0 have penetrated the vesicle. Not only the penetration rate was evaluated but also the mean squared radius of gyration of the arms over time. The arms of polymers whose backbone penetrated the membrane were less extended than the arms of the non-penetrated polymers, see Fig.5.31. This behaviour was observed independently of the stiffness of the lipids, see Fig.5.32. The difference of the mean squared radius of gyration of the arms of penetrated and non-penetrated polymers increased with increasing armlength. The reason for this observation could be that the extension of the arms of penetrated polymers is restricted in the direction of the vesicle since the arms cannot penetrate it.

The presented results show a strong dependency of the armlength and the penetration rate due to a shielding effect of the hydrophilic arms. A correlation of the stiffness of the lipids and the penetration rate could not be observed. Regarding the mean squared radius of gyration of the arms a methodical difference between penetrated and non-penetrated polymers could be observed.

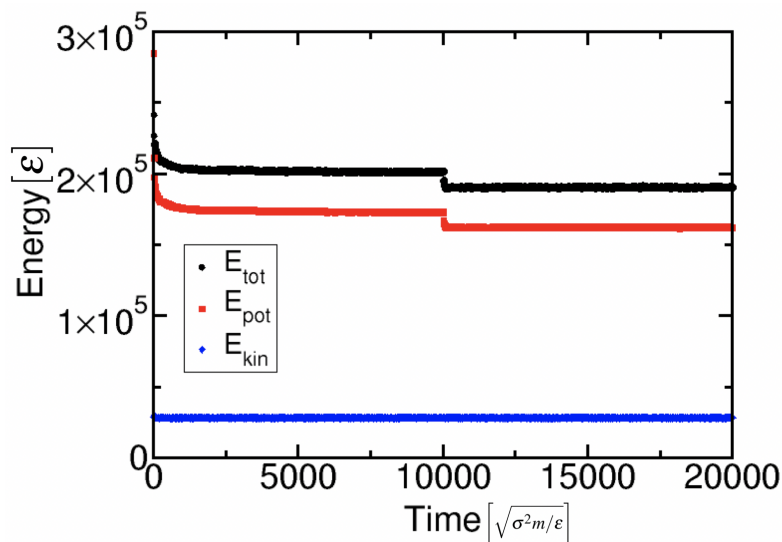


Figure 5.28: The total, potential and kinetic energy over the time.

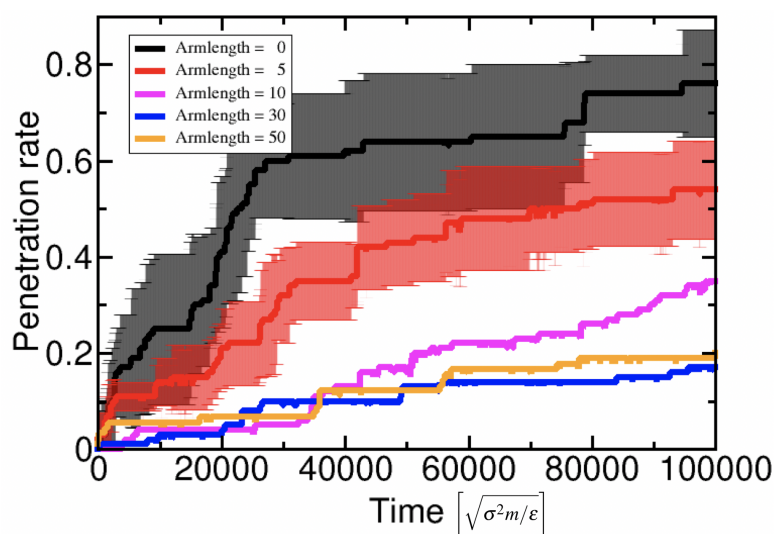


Figure 5.29: Penetration rate of bottle brush polymer type A with different arm-length. The lipids of the membrane had no bending strength $\kappa_{BEND} = 0$. For the armlengths $N_{arm}^{length} = 0$ and 5 error bars are shown.

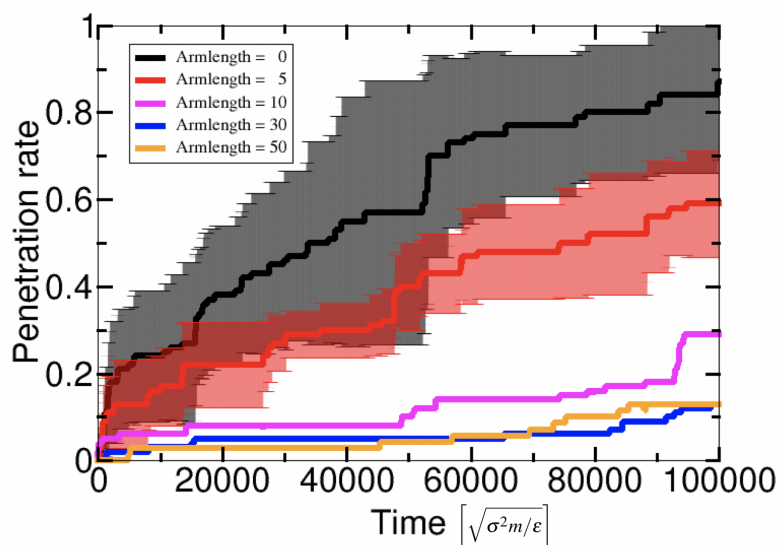


Figure 5.30: Penetration rate of bottle brush polymer type A with different arm-length. The lipids of the membrane had a bending strength of $\kappa_{BEND} = 1$. For the armlengths $N_{arm}^{length} = 0$ and 5 error bars are shown.

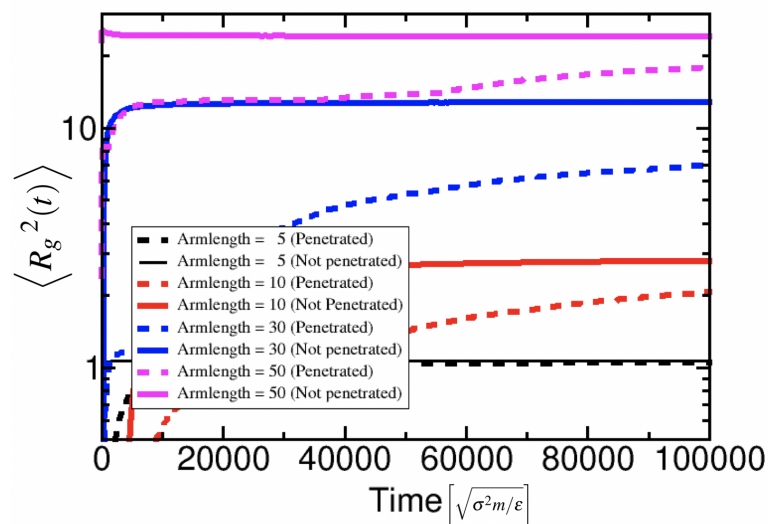


Figure 5.31: Mean-squared radius of gyration of the arms of penetrated and non-penetrated over time. No bending strength was applied to the lipids ($\kappa_{BEND} = 0$).

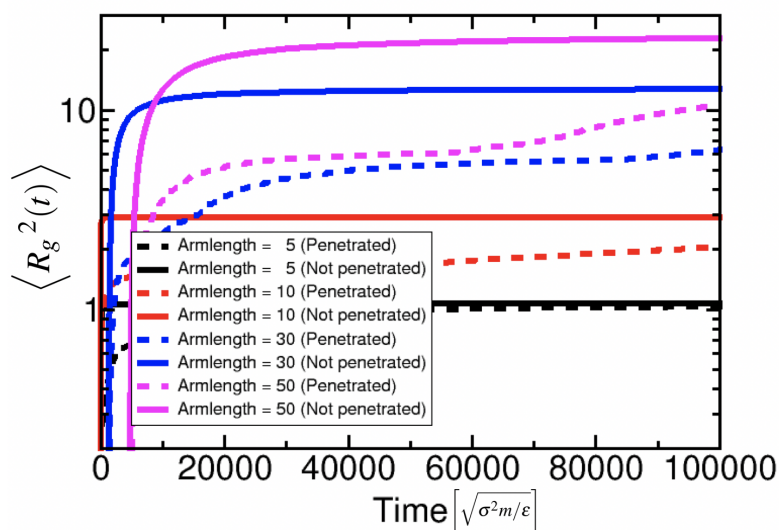


Figure 5.32: Mean-squared radius of gyration of the arms of penetrated and non-penetrated over time. A bending strength of $\kappa_{BEND} = 2.0$ was applied to the lipids.

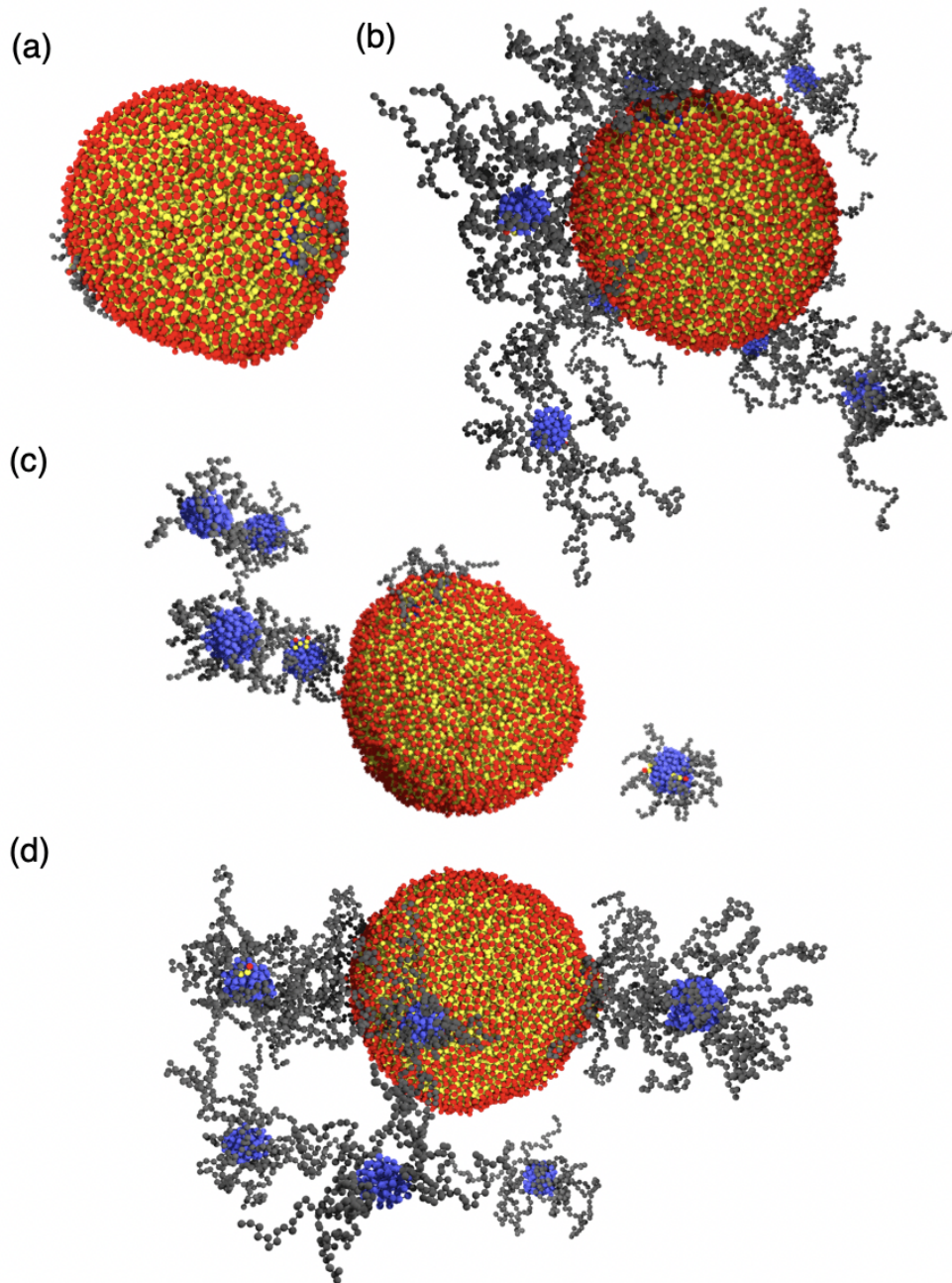


Figure 5.33: Snapshots of bottle brush polymers penetrating a vesicle composed of 5000 lipids: (a) $N_{arm}^{length} = 5$; (b) $N_{arm}^{length} = 50$; (c) $N_{arm}^{length} = 10$; (d) $N_{arm}^{length} = 30$.

6. Conclusion and Outlook

In this work, we performed three different studies. In a first study, the self-assembly of lipids was tested for a large parameter space. The self-assembly of amphiphilic copolymer gel-networks was investigated in a second study. In a third study the interaction of amphiphilic copolymers with hollow vesicles was explored. In the parameter study on the self-assembly of lipids, different forms of self-assembly were found. Besides hollow vesicles the vesicle-in-vesicle formation was the most interesting discovery since cell organells such as mitochondria show a similar structures [43]. Because this formation could be generated with high probability, further studies on that system could be of high interest. Scanning a larger parameter range would gain more knowledge about the self-assembled formations of lipids but is not possible due to computational limitations in this work. Here, using machine learning techniques could remedy so that only a small number of parameters is simulated and the remaining parameter range is filled up by applying machine learning methods [44].

The polymer networks showed as well very different forms of self-assembly. Besides well distinct clusters, connected clusters were observed. Moreover, for bottle brush polymer type A, membrane-like and vesicle formation could be observed. Vesicular formation could also be expected for bottle brush polymer type B with other topologies regarding the length of the backbone and the proportion of hydrophobicity [4]. To be more concrete, a shorter backbone with short arms attached and a hydrophobic proportion similar to that of lipids should result in membrane or vesicle formation choosing the right parameters for the temperature and density. Such polymer vesicles are of high interest in medical applications as drug carriers [45].

The interaction of amphiphilic copolymers with vesicles showed very interesting results. The star polymers showed that the higher the functionality is the less arms penetrate the vesicle due to steric effects at the center of the star. Moreover, a dependency of the number of hydrophobic particles at the end of the arms could be observed. The better the number matches with the number of hydrophobic particles inside the membrane, the easier it is for the polymers to penetrate. The penetration of bottle brush type A polymers showed a strong

dependency on the armlength and a shielding effect of the hydrophilic arms could be observed. Hence, the longer the arms are, the less the probability is that a backbone comes close enough to interact with the membrane. Another interesting observation was that the radius of gyration of the arms of the penetrated polymers was always lower than that of non-penetrated polymers. In further investigations it would be interesting to look at the stability of vesicles if the polymer concentration is increased. With a higher polymer concentration more penetration occurs which could destabilize the vesicle and destroy it.

In conclusion, it could be shown that the interaction of membranes with amphiphilic copolymers strongly depends on the polymer topology. Therefore, coarse-grained simulation studies give detailed insight into dynamic processes of the interaction between biological membranes and amphiphilic copolymers.

Bibliography

- [1] C. G. Palivan, R. Goers, A. Najer, X. Zhang, A. Car, and W. Meier. Bioinspired polymer vesicles and membranes for biological and medical applications. *Chem. Soc. Rev.*, **45**:377–411, 2015.
- [2] P. A. Beales, S. Khan, S. P. Muench, and L. J. C. Jeuken. Durable vesicles for reconstitution of membrane proteins in biotechnology. *Biochem. Soc. Trans.*, **45**:15–26, 2017.
- [3] X. Sun, S. Pei, J. F. Wang, P. Wang, Z. Liu, and J. Zhang. Coarse-grained molecular dynamics simulation study on spherical and tube-like vesicles formed by amphiphilic copolymers. *J. Polym. Sci. Pol. Phys.*, **55**(16):1220–1226, 2017.
- [4] I. Lyubimov, M. G. Wessels, and A. Jayaraman. Molecular dynamics simulation and prism theory study of assembly in solutions of amphiphilic bottlebrush block copolymers. *Macromolecules*, **51**(19):7586–7599, 2018.
- [5] R. Pasquino, H. Droghetti, P. Carbone, S. Mirzaagha, N. Grizzuti, and D. Marchisio. An experimental rheological phase diagram of a tri-block co-polymer in water validated against dissipative particle dynamics simulations. *Soft Matter*, **15**(6):1396–1404, 2019.
- [6] I. C. Gârlea, D. Jaramillo-Cano, and C. N. Likos. Self-organization of gel networks formed by block copolymer stars. *Soft Matter*, **306**:419, 2019.
- [7] S. Hu, C. Huang, H. Tsao, and Y. Sheng. Hybrid membranes of lipids and diblock copolymers: From homogeneity to rafts to phase separation. *Phy. Rev. E*, **99**:012403, 2019.
- [8] Y. Yang, Y. Sheng, and H. Tsao. Hybridization of Lipids to Monolayer and Bilayer Membranes of Triblock Copolymers. *J. Colloid Interface Sci.*, **544**:53–60, 2019.

- [9] B. Liebmann, S. Köppel, P. Königshofer, T. Bucsics, T. Reiberger, and P. Schwabl. Assessment of microplastic concentrations in human stool final results of a prospective study. In *Conference on Nano and microplastics in technical and freshwater systems*, 2018.
- [10] D. Bochicchio, E. Panizon, L. Monticelli, and G. Rossi. Interaction of hydrophobic polymers with model lipid bilayers. *Sci. Rep.*, **7**:6357, 2017.
- [11] K. Schumann and K. Siekmann. Soaps, Ullmann’s Encyclopedia of Industrial Chemistry. Weinheim: Wiley-VCH, 2005.
- [12] S. J. Marrink, A. H. de Vries, and A. E. Mark. Coarse Grained Model for Semiquantitative Lipid Simulations. *J. of Phys. Chem. B*, **108**(2):750–760, 2004.
- [13] I. R. Cooke, K. Kremer, and M. Deserno. Tunable generic model for fluid bilayer membranes. *Phys. Rev.*, **72**(1):011506, 2005.
- [14] T. Schindler, D. Kröner, and M. O. Steinhauser. On the dynamics of molecular self-assembly and the structural analysis of bilayer membranes using coarse-grained molecular dynamics simulations. *BBA-Biomembranes*, **1858**:1955–1963, 2016.
- [15] H. J. C. Berendsen, J. P. M. Postma, W. F. van Gunsteren, A. DiNola, and J. R. Haak. Molecular dynamics with coupling to an external bath. *J. Chem Phys*, **81**(8):3684–3690, 1984.
- [16] M. P. Allen. Algorithms for brownian dynamics. *Mol. Phys.*, **47**(3):599–601, 1982.
- [17] M. Doi and S. F. Edwards. *The Theory of Polymer Dynamics*. Clarendon Press, Oxford, 1986.
- [18] M. O. Steinhauser. Computational multiscale modeling of fluids and solids. Springer, 2017.
- [19] J. D. Weeks, D. Chandler, and H. C. Andersen. Role of Repulsive Forces in Determining the Equilibrium Structure of Simple Liquids. *J. Chem. Phys.*, **54**(12):5237–5247, 2003.
- [20] P. Košován, J. Kuldová, Z. Limpouchová, K. Procházka, E. B. Zhulina, and O. V. Borisov. Amphiphilic Graft Copolymers in Selective Solvents: Molecular Dynamics Simulations and Scaling Theory. *Macromolecules*, **42**(17):6748–6760, 2009.

- [21] I. R. Cooke and M. Deserno. Solvent-free model for self-assembling fluid bilayer membranes: Stabilization of the fluid phase based on broad attractive tail potentials. *J. Chem. Phys.*, **123**(22):224710, 2005.
- [22] M. O. Steinhauser, M. Kühn 3rd Intl Conference on Multiscale, and 2006. Modeling of shock-wave failure in brittle materials. pages 380–382, 2006.
- [23] M. O. Steinhauser, J. Schneider, and A. Blumen. Simulating dynamic crossover behavior of semiflexible linear polymers in solution and in the melt. *J. Chem. Phys.*, **130**(16):164902, 2009.
- [24] M. O Steinhauser. Computational methods in polymer physics. *Recent Res. Devel. Physics*, **7**(59-97):26, 2006.
- [25] M. O. Steinhauser. Static and dynamic scaling of semiflexible polymer chains—a molecular dynamics simulation study of single chains and melts. *Mechanics of Time-Dependent Materials*, **12**(4):291–312, 2008.
- [26] M. O. Steinhauser. *Computer Simulation in Physics and Engineering*. 2012.
- [27] M. N. Rosenbluth and A. W. Rosenbluth. Monte Carlo Calculation of the Average Extension of Molecular Chains. *J. Chem. Phys.*, **23**(2):356–359, 1955.
- [28] L. Boltzmann. Vorlesungen über Gastheorie: Th. Theorie van der Waals'; Gase mit zusammengesetzten Molekülen; Gasdissociation; Schlussbemerkungen, 1898.
- [29] B. J. Alder and T. E. Wainwright. Phase transition for a hard sphere system. *J. Chem. Phys.*, **27**:356–359, 1957.
- [30] L. Verlet. Computer "Experiments" on Classical Fluids. I. Thermodynamical Properties of Lennard-Jones Molecules. *Phys. Rev.*, **159**(1):98–103, 1967.
- [31] C. K. Birdsall and A. B. Langdon. *Plasma Physics via Computer Simulation*. 1991.
- [32] L. Verlet. Computer "Experiments" on Classical Fluids. II. Equilibrium Correlation Functions. *Phys. Rev.*, **165**(1):201–214, 1968.
- [33] R. Reissig. Liapunov, stability of motion. *J. of Appl. Math. and Mech.*, **48**:140–140, 1968.
- [34] M. O. Steinhauser and S. Hiermaier. A Review of Computational Methods in Materials Science: Examples from Shock-Wave and Polymer Physics. *Int. J. Mol. Sc.*, **10**(12):5135–5216, 2009.

- [35] J. MacQueen et al. Some methods for classification and analysis of multivariate observations. In *Proceedings of the fifth Berkeley symposium on mathematical statistics and probability*, volume 1, pages 281–297, 1967.
- [36] R. R. Sokal. A statistical method for evaluating systematic relationships. *Univ. Kansas, Sci. Bull.*, **38**:1409–1438, 1958.
- [37] J. H. Ward Jr. Hierarchical grouping to optimize an objective function. *J. Am. Stat. Assoc.*, **58**(301):236–244, 1963.
- [38] L. Kaufman and P. J Rousseeuw. *Finding groups in data: an introduction to cluster analysis*, volume **344**. John Wiley & Sons, 2009.
- [39] A. J. Moreno and F. L. Verso. Computational investigation of microgels: synthesis and effect of the microstructure on the deswelling behavior. *Soft Matter*, **14**(34):7083–7096, 2018.
- [40] M. Ester, H. P. Kriegel, J. Sander, and X. Xu. A density-based algorithm for discovering clusters in large spatial databases with noise. In *Kdd*, volume **96**, pages 226–231, 1996.
- [41] B. Alberts, D. Bray, K. Hopkin, A. D. Johnson, J. Lewis, M. Raff, K. Roberts, and P. Walter. *Essential cell biology*. Garland Science, 2013.
- [42] M. O. Steinhauser. A molecular dynamics study on universal properties of polymer chains in different solvent qualities. Part I. A review of linear chain properties. *J. Chem. Phys.*, **122**(9):094901–1–094901–13, 2005.
- [43] B. Alberts, A. Johnson, J. Lewis, M. Raff, K. Roberts, and P. Walter. *Molecular biology of the cell*. Garland Science, 2002.
- [44] E. PL. Van Nieuwenburg, Y. Liu, and S.D. Huber. Learning phase transitions by confusion. *Nat. Phys.*, **13**(5):435, 2017.
- [45] R. Verduzco, X. Li, S. L. Pesek, and G. E. Stein. Structure, function, self-assembly, and applications of bottlebrush copolymers. *Chem. Soc. Rev.*, **44**(8):2405–2420, 2015.

Appendices

A. Vesicle Formation

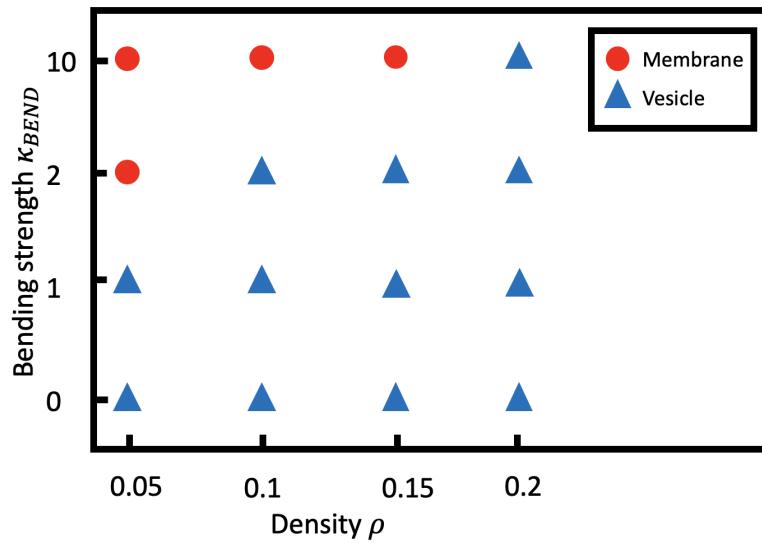


Figure A.1: Phase diagram of the bending strength κ_{BEND} and the density ρ at fixed temperature $T = 1.0$ and hydrophobic range $h_c = 1.5$ of a system with $N_{lipid} = 1000$ lipids.

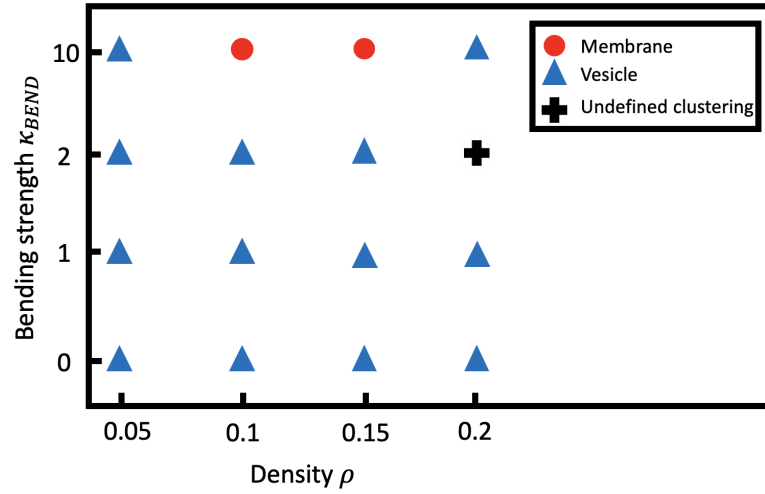


Figure A.2: Phase diagram of the bending strength κ_{BEND} and the density ρ at fixed temperature $T = 1.5$ and hydrophobic range $h_c = 1.8$ of a system with $N_{lipid} = 1000$ lipids.

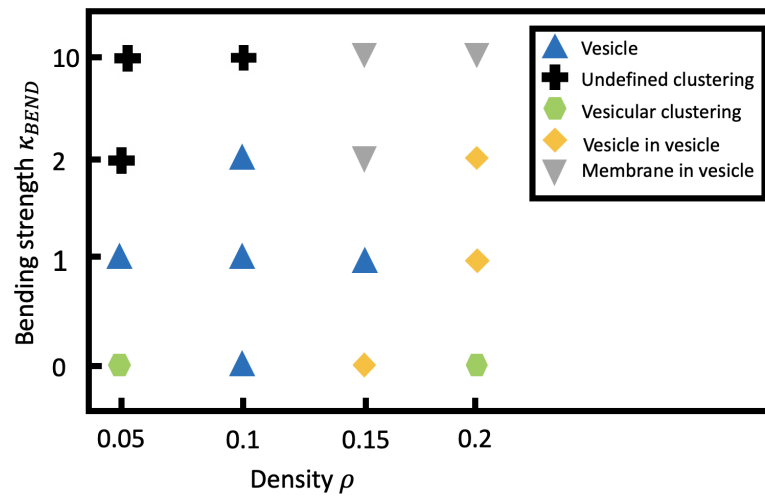


Figure A.3: Phase diagram of the bending strength κ_{BEND} and the density ρ at fixed temperature $T = 1.0$ and hydrophobic range $h_c = 1.5$ of a system with $N_{lipid} = 5000$ lipids.

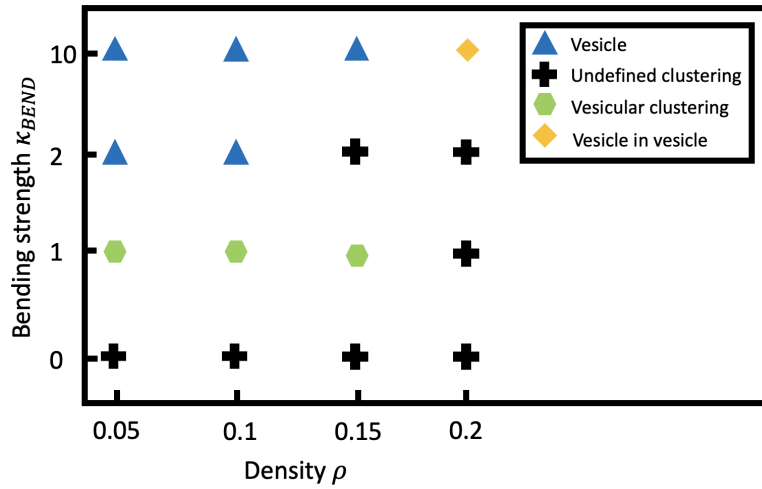


Figure A.4: Phase diagram of the bending strength κ_{BEND} and the density ρ at fixed temperature $T = 1.5$ and hydrophobic range $h_c = 1.8$ of a system with $N_{lipid} = 5000$ lipids.

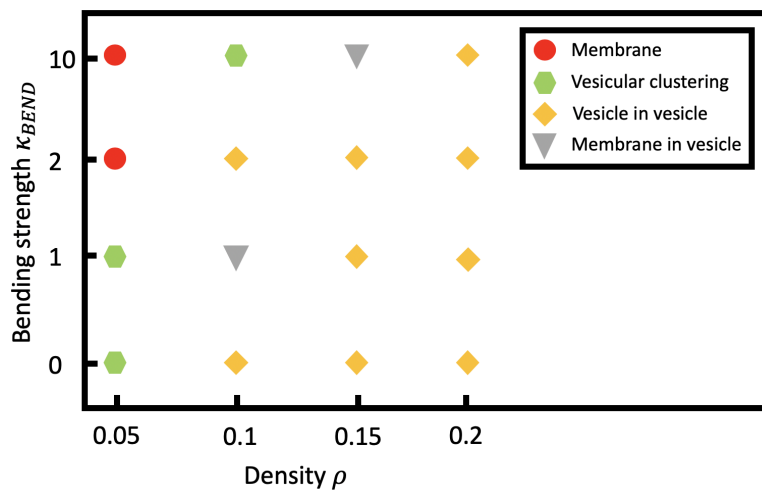


Figure A.5: Phase diagram of the bending strength κ_{BEND} and the density ρ at fixed temperature $T = 1.0$ and hydrophobic range $h_c = 1.5$ of a system with $N_{lipid} = 10000$ lipids.

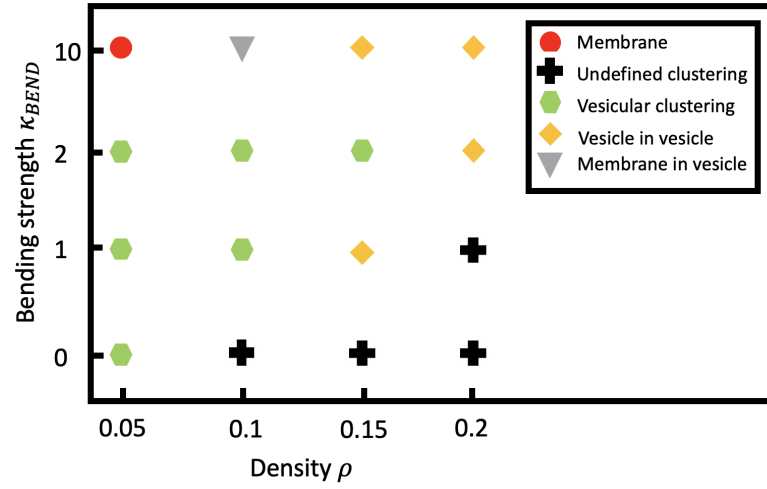


Figure A.6: Phase diagram of the bending strength κ_{BEND} and the density ρ at fixed temperature $T = 1.5$ and hydrophobic range $h_c = 1.8$ of a system with $N_{lipid} = 10000$ lipids.

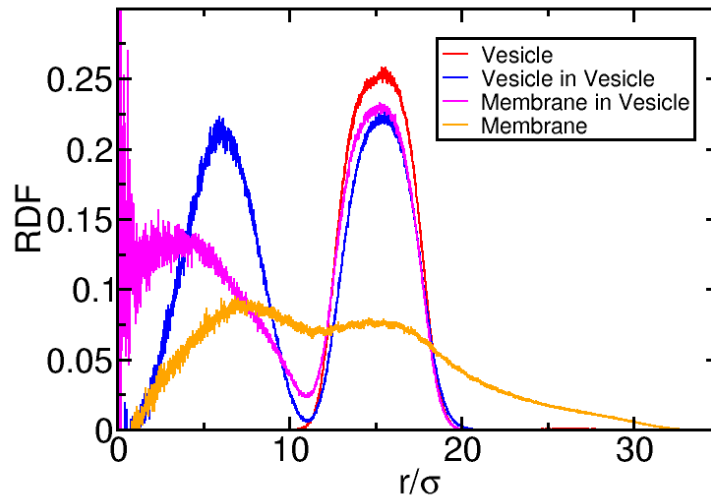


Figure A.7: RDF of different structures found in systems consisting of 5000 lipids.

B. Amphiphilic Copolymers

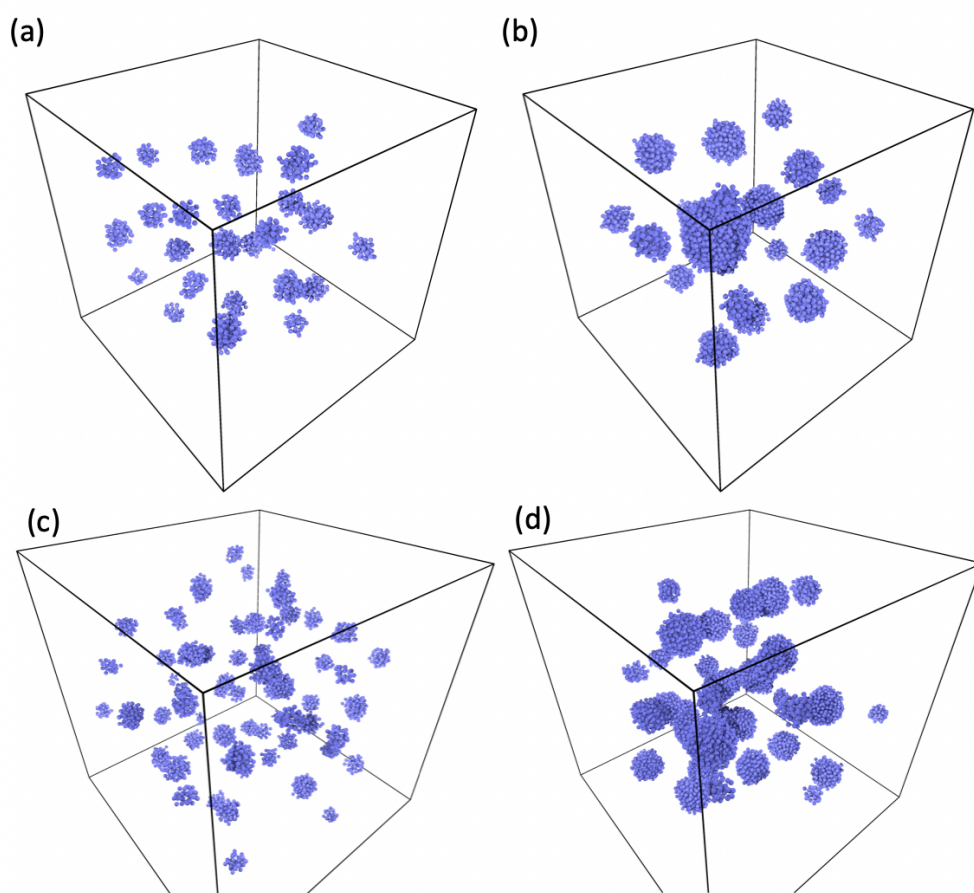


Figure B.1: Snapshots of star polymer networks: (a) $f = 4$ and $N_{hydrophobic} = 4$; (b) $f = 4$ and $N_{hydrophobic} = 10$; (c) $f = 9$ and $N_{hydrophobic} = 4$; (d) $f = 9$ and $N_{hydrophobic} = 10$.

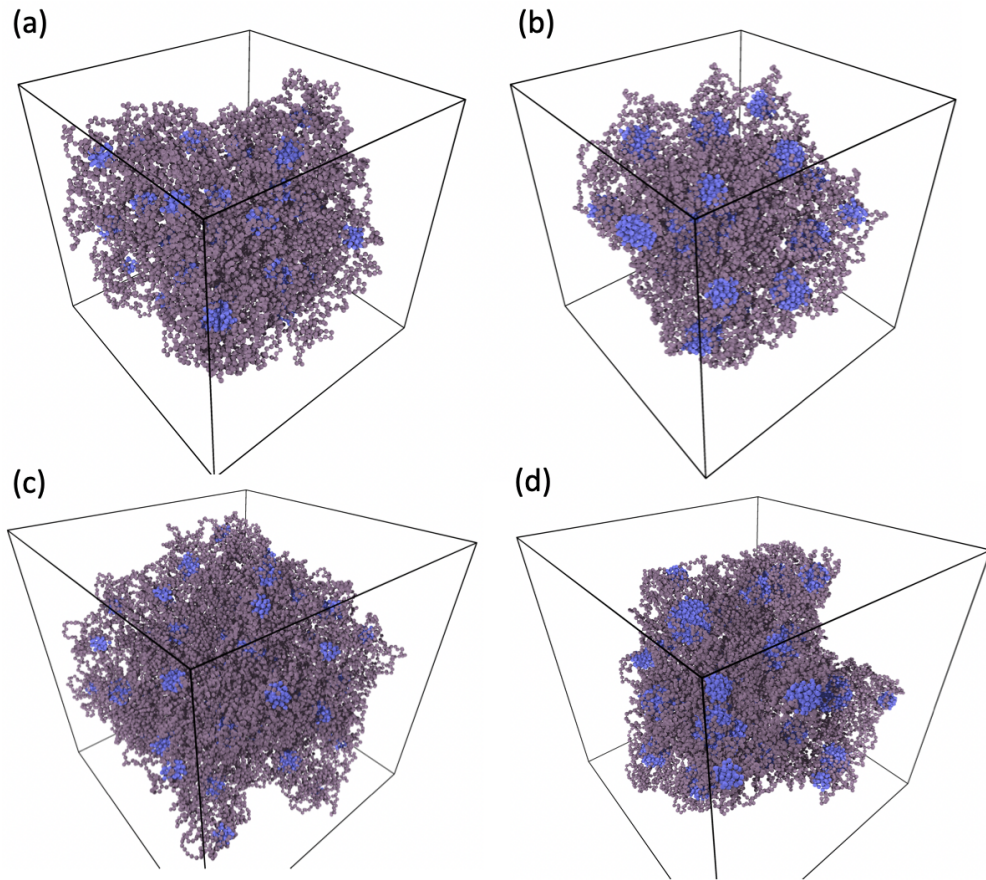


Figure B.2: Snapshots of star polymer networks: (a) $f = 4$ and $N_{hydrophobic} = 4$; (b) $f = 4$ and $N_{hydrophobic} = 10$; (c) $f = 9$ and $N_{hydrophobic} = 4$; (d) $f = 9$ and $N_{hydrophobic} = 10$

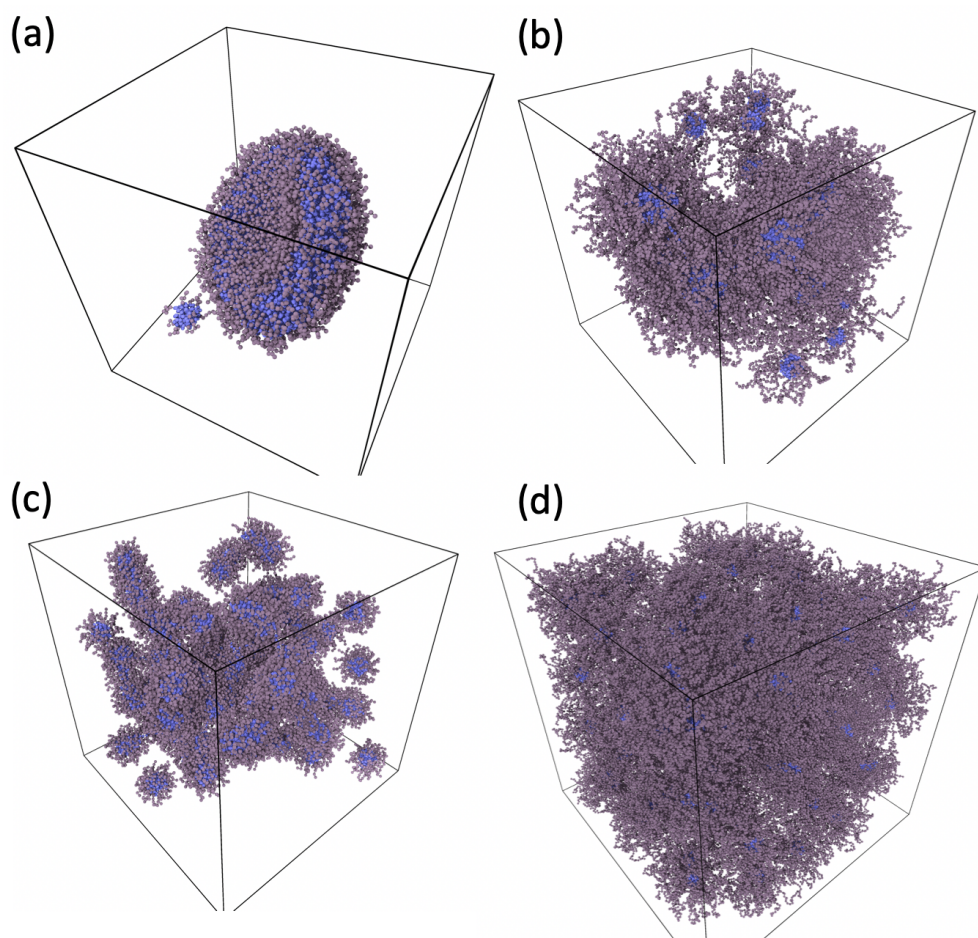


Figure B.3: Snapshots of a bottle brush polymer network type A: (a) $N_{arm} = 10$ and $N_{arm}^{length} = 5$; (b) $N_{arm} = 10$ and $N_{arm}^{length} = 5$; (c) $N_{arm} = 50$ and $N_{arm}^{length} = 5$; (d) $N_{arm} = 50$ and $N_{arm}^{length} = 30$.

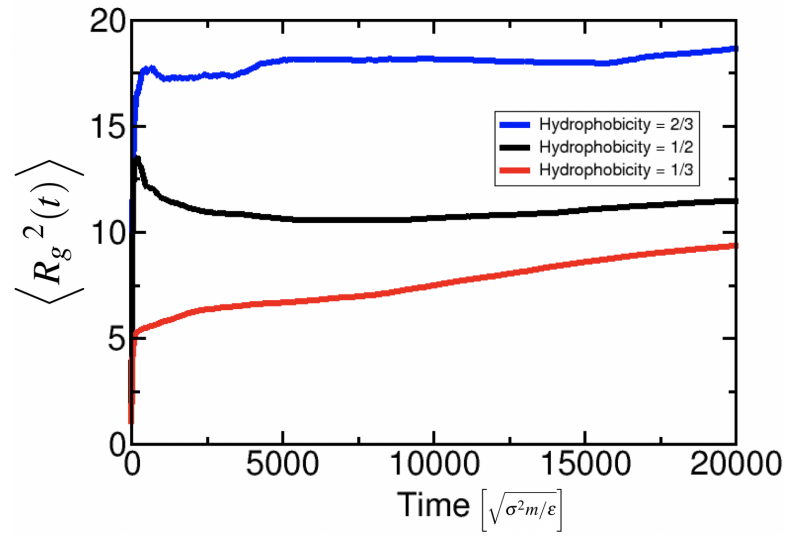


Figure B.4: Mean-squared radius of gyration of the clusters over time of different hydrophobic ratios of a bottle brush molecule with $N_{arm} = 10$ and $N_{arm}^{length} = 5$.

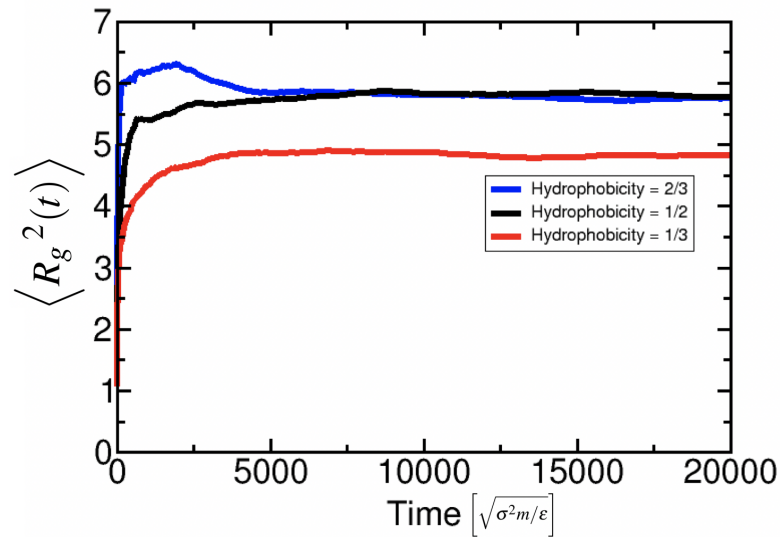


Figure B.5: Mean-squared radius of gyration of the clusters over time of different hydrophobic ratios of a bottle brush molecule with $N_{arm} = 10$ and $N_{arm}^{length} = 30$.

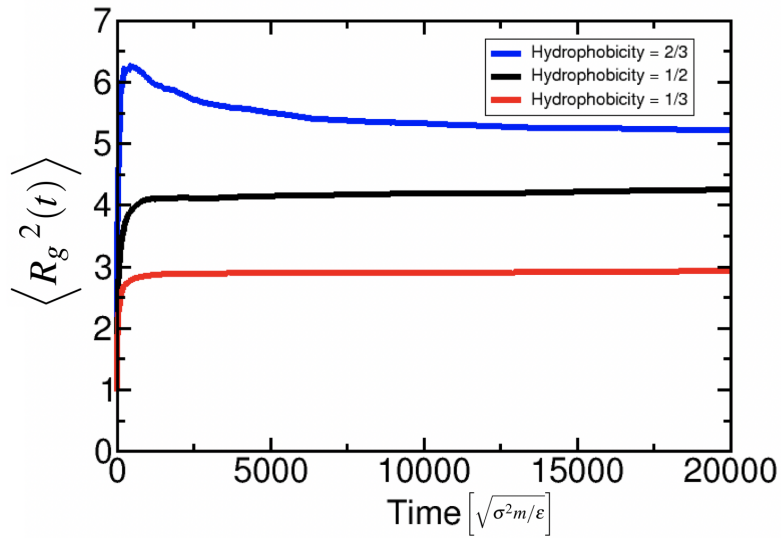


Figure B.6: Mean-squared radius of gyration of the clusters over time of different hydrophobic ratios of a bottle brush molecule with $N_{arm} = 50$ and $N_{arm}^{length} = 5$.

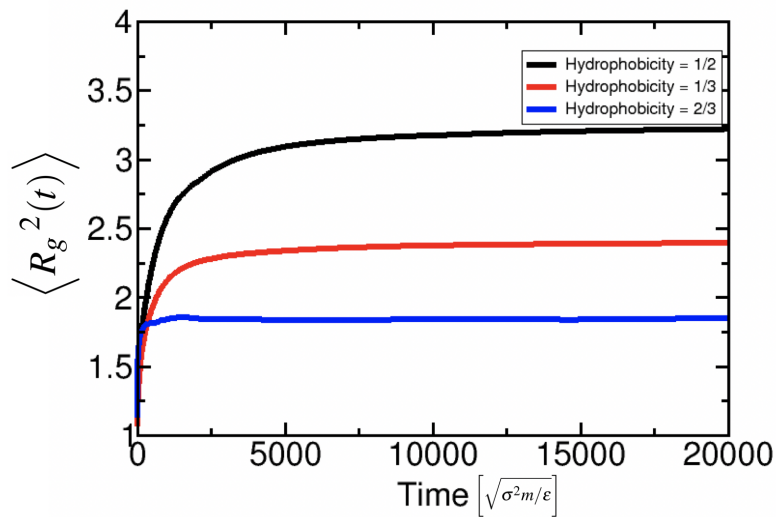


Figure B.7: Mean-squared radius of gyration of the clusters over time of different hydrophobic ratios of a bottle brush molecule with $N_{arm} = 50$ and $N_{arm}^{length} = 30$.

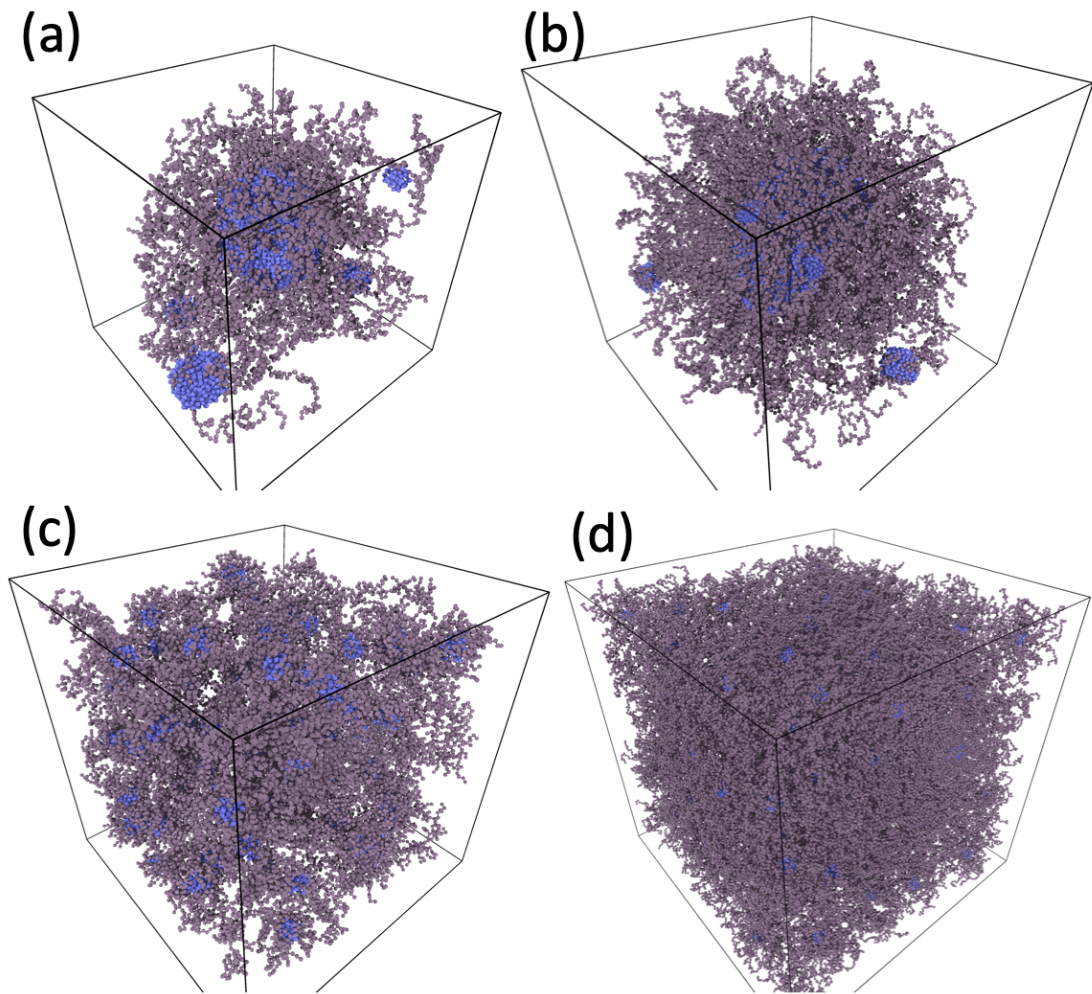


Figure B.8: Snapshots of a bottle brush molecule type B2 which has a hydrophobic ratio of 1/3: (a) $N_{arm} = 10$ and $N_{arm}^{length} = 5$; (b) $N_{arm} = 10$ and $N_{arm}^{length} = 5$; (c) $N_{arm} = 50$ and $N_{arm}^{length} = 5$; (d) $N_{arm} = 50$ and $N_{arm}^{length} = 30$.

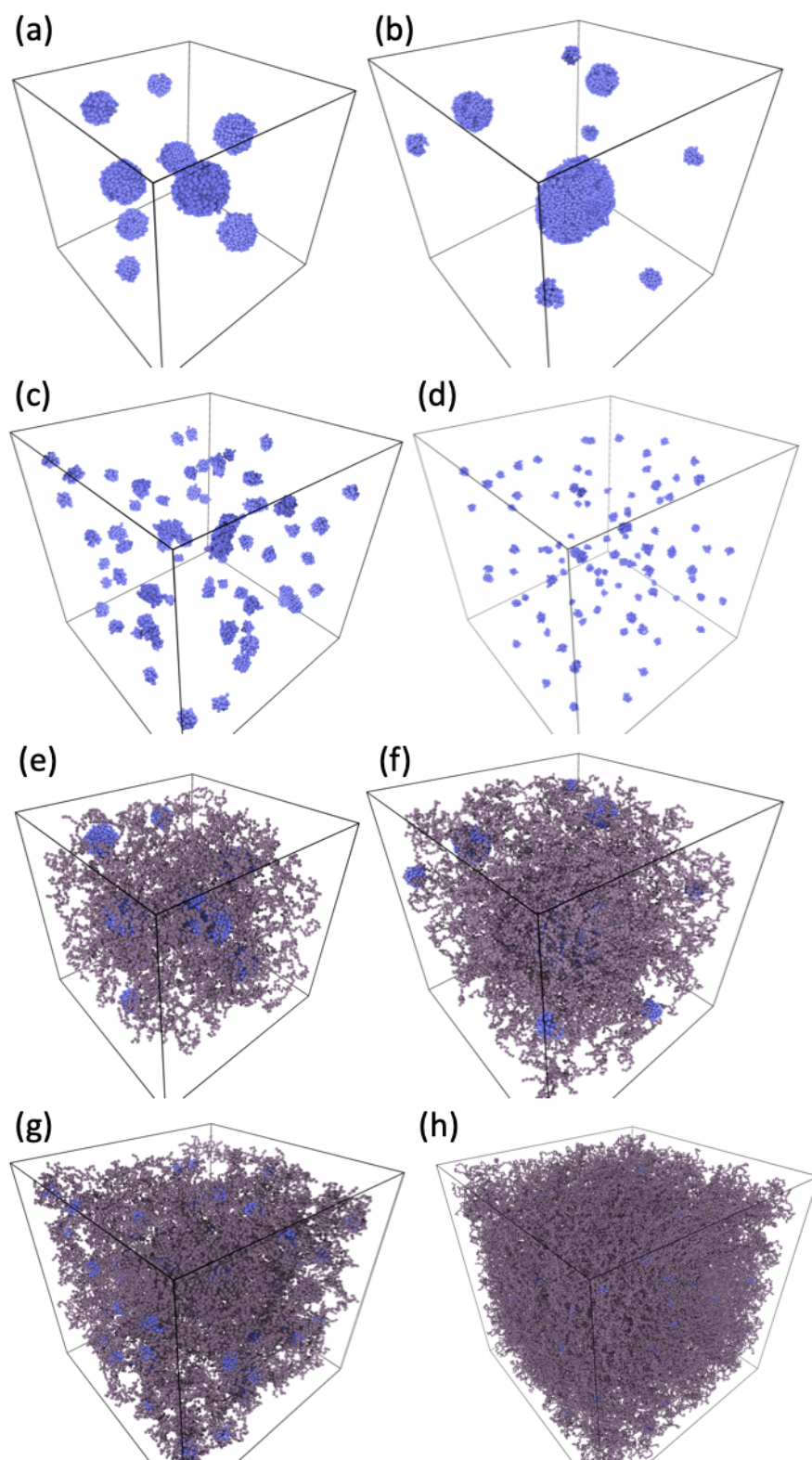


Figure B.9: Snapshots of a bottle brush molecule type B2 which has a hydrophobic ratio of 1/3: (a) and (e) $N_{arm} = 10$ and $N_{arm}^{length} = 5$; (b) and (f) $N_{arm} = 10$ and $N_{arm}^{length} = 30$; (c) and (g) $N_{arm} = 50$ and $N_{arm}^{length} = 5$; (d) and (h) $N_{arm} = 50$ and $N_{arm}^{length} = 30$.

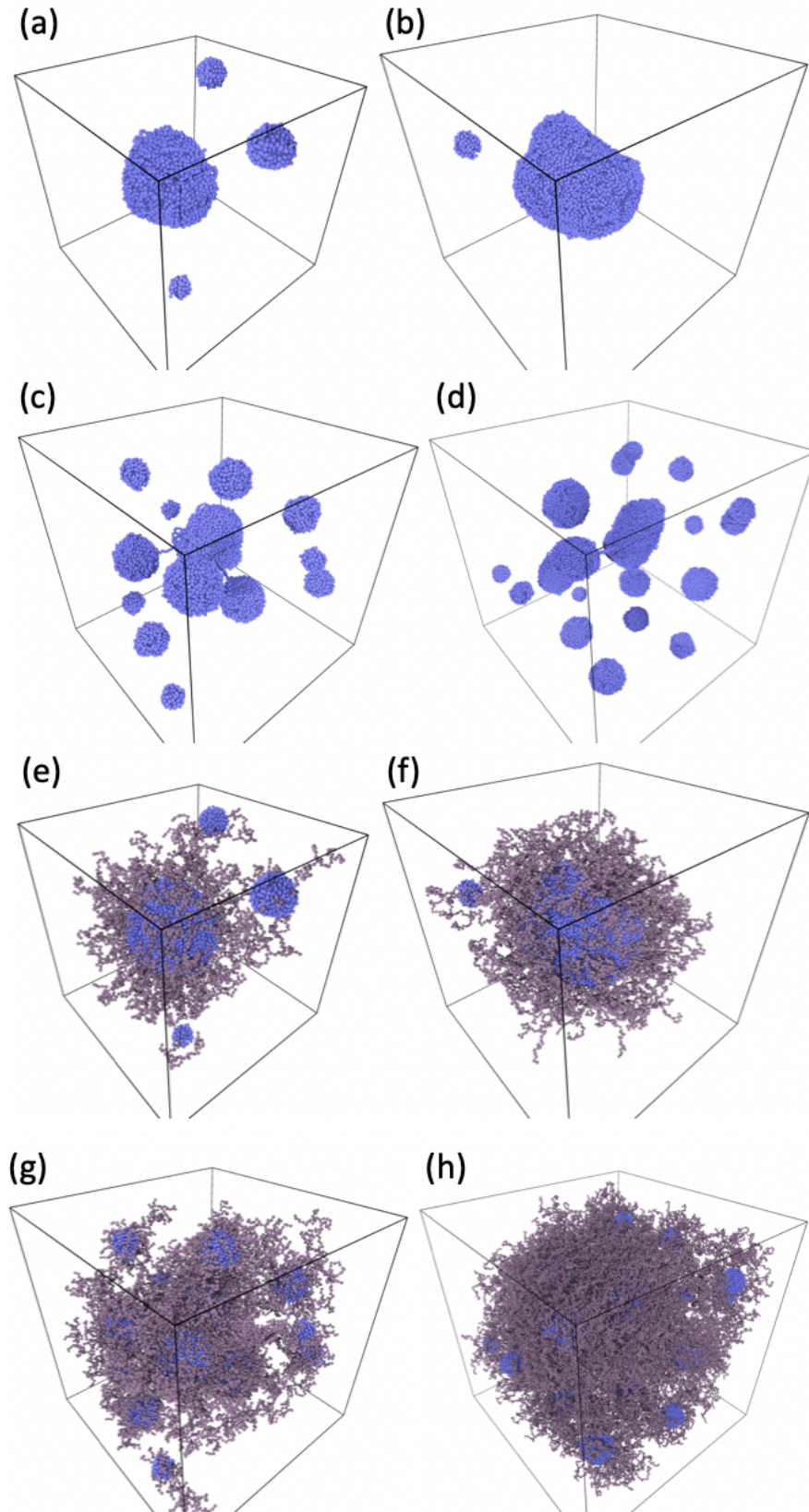


Figure B.10: Snapshots of a bottle brush molecule type B3 which has a hydrophobic ratio of 2/3: (a) and (e) $N_{arm} = 10$ and $N_{arm}^{length} = 5$; (b) and (f) $N_{arm} = 10$ and $N_{arm}^{length} = 5$; (c) and (g) $N_{arm} = 50$ and $N_{arm}^{length} = 5$; (d) and (h) $N_{arm} = 50$ and $N_{arm}^{length} = 30$.

C. Hybrid Systems

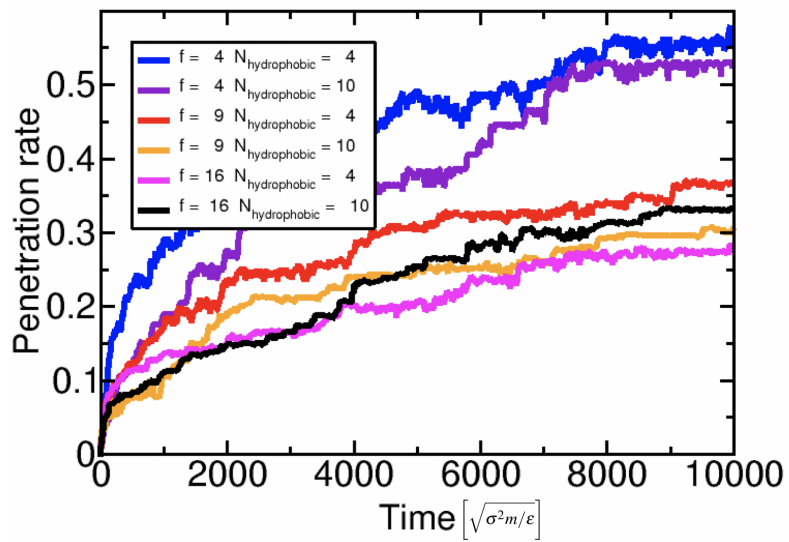


Figure C.1: Penetration rate of star polymers into vesicles made of lipids with a bending strength of $\kappa_{BEND} = 1.0$

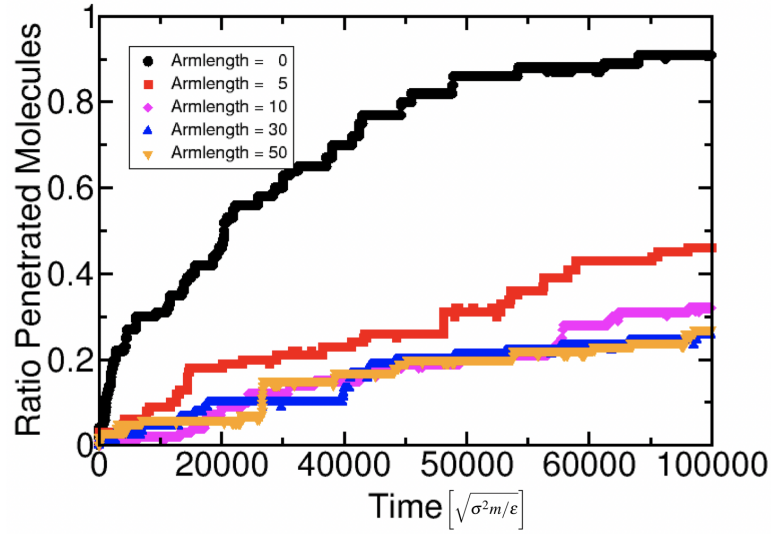


Figure C.2: Penetration rate of bottle brush molecules into vesicles containing lipids with a bending strength of $\kappa_{BEND} = 1.0$

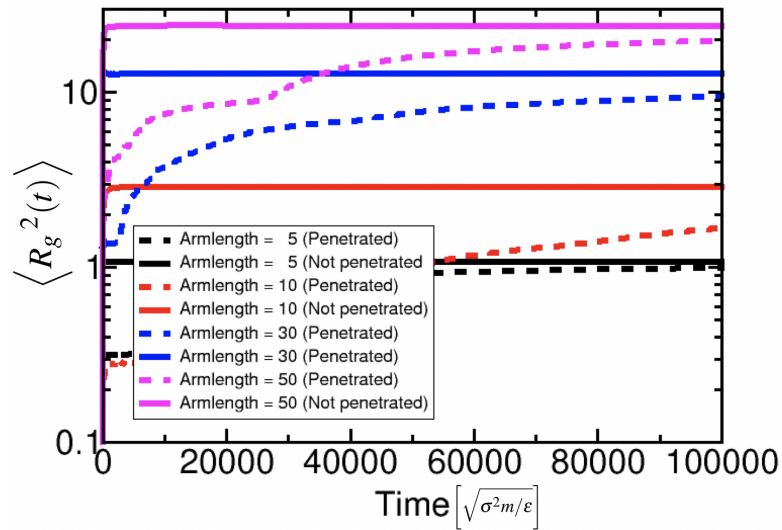


Figure C.3: Mean-squared radius of gyration of the arms of penetrated and non-penetrated bottle brush polymers. To the lipids of the vesicle a bending strength of $\kappa_{BEND} = 1.0$ was applied.